Deltares

Enabling Delta Life

Hydrodynamics and bedforms on the Dutch lower shoreface

Analysis of ADCP, ADV, and SONAR observations

Hydrodynamics and bedforms on the Dutch lower shoreface

Analysis of ADCP, ADV, and SONAR observations

Reinier Schrijvershof
Laura Brakenhoff
Bart Grasmeijer

Deltares

Title
Hydrodynamics and bedforms on the Dutch lower shoreface

Client	Project	Attribute	Pages
Rijkswaterstaat Water, Verkeer en Leefomgeving, RIJSWIJK	1220339-007	1220339-007-ZKS-0009	58

Keywords
Coastal Genesis 2.0 (Kustgenese 2.0), lower shoreface, field observations, wave orbital velocity, wave skewness, wave asymmetry, residual currents, small-scale bedforms, bedform predictors

Summary
Field observations of currents, waves, and bedforms were gathered in four field campaigns as part of the Coastal Genesis 2.0 (Kustgenese 2.0, KG2) programme. The field campaigns, situated along the Dutch lower shoreface (~8 m up to ~20 m water depth), were carried out to study lower shoreface hydro- and morphodynamic processes. This report describes a data analysis of the observed hydrodynamics and bedforms.

The field observations are used to study the temporal and spatial variability of the near-bed orbital wave motion, residual (non-tide driven) flow, and small-scale bedforms at different depths and locations, and under varying conditions on the lower shoreface. The orbital wave motion is derived from high frequency (16 Hz) ADV observations at approximately 0.5 m above the bed, the residual flow is estimated by filtering low-frequency signals from the ADCP measured current velocity profiles, and bedform types and dimensions are derived from very high-resolution digital elevation models (DEM) measured with an acoustic SONAR.

The results show that the wave-induced orbital velocity can reach ~1 m/s at the lower part of the lower shoreface and this value is exceeded in shallower parts during energetic wave conditions (H_s > 4 m, H_s/h = ~0.3). Corresponding to linear wave theory, and thus demonstrating its validity for the studied environment, the orbital velocity scales linearly with the local significant wave height, which increases at shallower depths. Waves are not asymmetric on the lower shoreface but become skewed with energetic wave conditions, which is described well by the Ruessink et al. (2012) formulation for wave skewness and asymmetry.

Besides the wave-induced oscillatory motion there is a net residual current present at the lower shoreface, driven by non-breaking wave conditions, wind and possibly density gradients (although not studied). During mild wind and wave conditions, the strength is a few dm/s in longshore direction and a few cm/s in cross-shore direction. With energetic wind and wave conditions the longshore current is observed to reach up to ~0.5 m/s and the cross-shore current up to ~0.4 m/s. During these conditions the cross-shore velocity profile is in landward direction over the complete depth, which cannot be explained well from the present conceptual understanding of lower shoreface hydrodynamics.

Deltares

Title
Hydrodynamics and bedforms on the Dutch lower shoreface

Client	Project	Attribute	Pages
Rijkswaterstaat Water, Verkeer en Leefomgeving, RIJSWIJK	1220339-007	1220339-007-ZKS-0009	58

The hydrodynamic conditions observed during the field campaigns range between the full spectrum of possible sediment motion conditions (no motion, wave-current dominated, and sheet flow). The accompanying observed bedforms range between 0.01 – 0.03 m in height (η) and between 0.08 – 0.20 m in length (λ). Moving up the lower shoreface (decreasing water depth) the bedforms become shorter, steeper (equal height), and more three-dimensional. These changes in bedform dimensions can be related to an increase of the wave orbital motion at shallower depths. The temporal change, however, is far more constant then expected, which is also the reason for a poor performance of bedform predictors.

Version	Date	Author	Initials	Review	Initials	Approval	Initials
0.1	July 2019	Reinier Schrijvershof Laura Brakenhoff Bart Grasmeijer		Robert McCall	RM	Frank Hoozemans	

Status
Final

Deltares

Title
Hydrodynamics and bedforms on the Dutch lower shoreface

Client	Project	Attribute	Pages
Rijkswaterstaat Water, Verkeer en Leefomgeving, RIJSWIJK	1220339-007	1220339-007-ZKS-0009	58

Nederlandse samenvatting
Gedurende vier veldcampagnes, uitgevoerd als onderdeel van het Kustgenese 2.0 (KG2) programma, zijn er metingen verricht naar stroming, golven en beddingvormen. De veldcampagnes, gesitueerd langs de Nederlandse diepe vooroever (~8 tot ~20 m waterdiepte) zijn uitgevoerd om de hydro- en morfodynamische processen op de diepe vooroever in detail te bestuderen. Dit rapport beschrijft een data-analyse van de waargenomen hydrodynamica en beddingvormen.

De veldmetingen zijn gebruikt om de temporele en ruimtelijke variabiliteit van de golfgedreven orbitaalsnelheden bij de bodem, de residuele (niet-getijgedreven) stroming en de beddingvormen te bestuderen op verschillende dieptes en locaties van de diepe vooroever en onder variërende condities. De golfgedreven orbitaalsnelheden zijn afgeleid van hoogfrequente (16 Hz) ADV metingen op ongeveer 0,5 m boven de bodem. De residuele stroming is geschat door van de gemeten stromingsprofielen (gemeten met een ADCP) de laagfrequente (getijgedreven) variaties uit te filteren. De vorm en dimensies van de beddingvormen zijn afgeleid van hoge resolutie bodemopnames, gemeten met een akoestische SONAR.

De resultaten van de analyse laten zien dat de golfgedreven orbitaalsnelheden bij de bodem een grootte van ongeveer ~1 m/s kunnen bereiken op het lagere gedeelte van de diepere vooroever. Tijdens energetische wind- en golfcondities (H_s > 4 m, H_s/h = ~0,3) kan de grootte zelfs meer dan 1 m/s zijn op de ondiepere gedeelten van de diepe vooroever. De gemeten orbitaalsnelheid schaalt met de lokale gemeten significante golfhoogte (overeenkomstig met lineaire golftheorie). Over de gehele diepe vooroever zijn golven nooit asymmetrisch maar worden wel scheef (skewed) tijdens energetische golfcondities. Deze golftransformatie wordt goed beschreven aan de hand van de Ruessink et al. (2012) formulering.

Naast de golfgedreven orbitaalbeweging is er een netto residuele stroming aanwezig op de diepe vooroever. Deze stroming wordt gedreven door niet-brekende golven, wind en mogelijk ook dichtheidsgradiënten (maar dit is niet onderzocht). Gedurende milde wind- en golfcondities is de sterkte van de stroming enkele dm/s in kustlangse richting, en enkele cm/s in kustdwarse richting. Tijdens meer energetische condities kan de kustlangse stroming een sterkte van ~0,5 m/s en de kustdwarse stroming een sterkte van ~0,4 m/s bereiken. Tijdens deze condities is het kustdwarse stromingsprofiel over de gehele diepte in landwaartse richting. Dit komt niet overeen met de theorie en is een aanvulling op het huidige conceptuele model van de hydrodynamische processen op de diepe vooroever.

De hydrodynamische condities die gemeten zijn tijdens de veldcampagnes variëren over het compleet mogelijke spectrum voor sedimenttransport (geen beweging, golf- en stromingsdominantie, zeer hoge mobiliteit – sheet flow). De beddingvormen die tijdens deze condities gemeten zijn variëren tussen 0,01 – 0,03 m in hoogte (η) en tussen 0,08 – 0,20 m in lengte (λ). Naar ondiepere gedeelte van de diepe vooroever toe worden de beddingvormen korter, steiler (gelijke hoogte) en meer driedimensionaal. Deze veranderingen in beddingvormdimensies kunnen gerelateerd worden aan een toename van de golfgedreven orbitaalbeweging met afnemende waterdiepte. De verandering van de dimensies in de tijd is echter veel constanter dan verwacht, wat ook de reden is dat beddingvormvoorspellers niet goed presteren.

Contents

1 Introduction

1.1 Kustgenese 2.0

The Dutch coastal policy aims for a safe, economically strong and attractive coast (Deltaprogramma, 2015). This is achieved by maintaining the part of the coast that supports these functions; the coastal foundation. In 2020 the Dutch Ministry of Infrastructure and Environment will decide on the future nourishment volume required to maintain the coastal foundation. The Kustgenese 2.0 (KG2, Coastal Genesis 2.0) programme is aimed at providing the knowledge to enable this decision-making. The scope of the KG2 project, commissioned by Rijkswaterstaat to Deltares, is determined by three main questions (Van Oeveren - Theeuwes et al., 2017):

1 What are possibilities for an alternative offshore boundary of the coastal foundation?
2 How much sediment is required for the coastal foundation to grow with sea level rise?
3 What are the possibilities for large scale nourishments along the interrupted coastline (inlets), and what could be the added value compared to regular nourishments?

The Deltares KG2 subproject “Diepe Vooroever” (DV, lower shoreface) contributes to the first two main research questions and the subproject “Zeegaten” (ZG, tidal inlets) contributes to the third main research question of KG2. Furthermore, the KG2 project cooperates with the SEAWAD STW research project, led by Delft University of Technology, Utrecht University and University of Twente. SEAWAD is developing the system knowledge and tools to predict the effects of mega-nourishments on the Ameland ebb-tidal delta on morphology and ecology (benthos distribution).

The KG2-DV project is studying the morphodynamics of the Dutch lower shoreface because the offshore limit of the lower shoreface (NAP -20 m depth) is defined as the offshore boundary of the coastal foundation. The onshore limit is formed by the landward edge of the dune area (closed coast) and by the tidal inlets (open coast) and the national borders with Belgium and Germany are the lateral boundaries (Figure 1.1). The coastal foundation is maintained by means of sand nourishments and the total nourishment volume is about 12 million m^3/year since 2000. It is crucial to quantitively understand sediment transport rates on the lower shoreface to make a substantiated decision on the first KG2 research question. However, the relevant driving processes on the lower shoreface are poorly understood. Hence, the KG2-DV project studies in particular the net cross-shore sand transport as a function of depth, on the basis of field observations, numerical modelling and system and process knowledge.

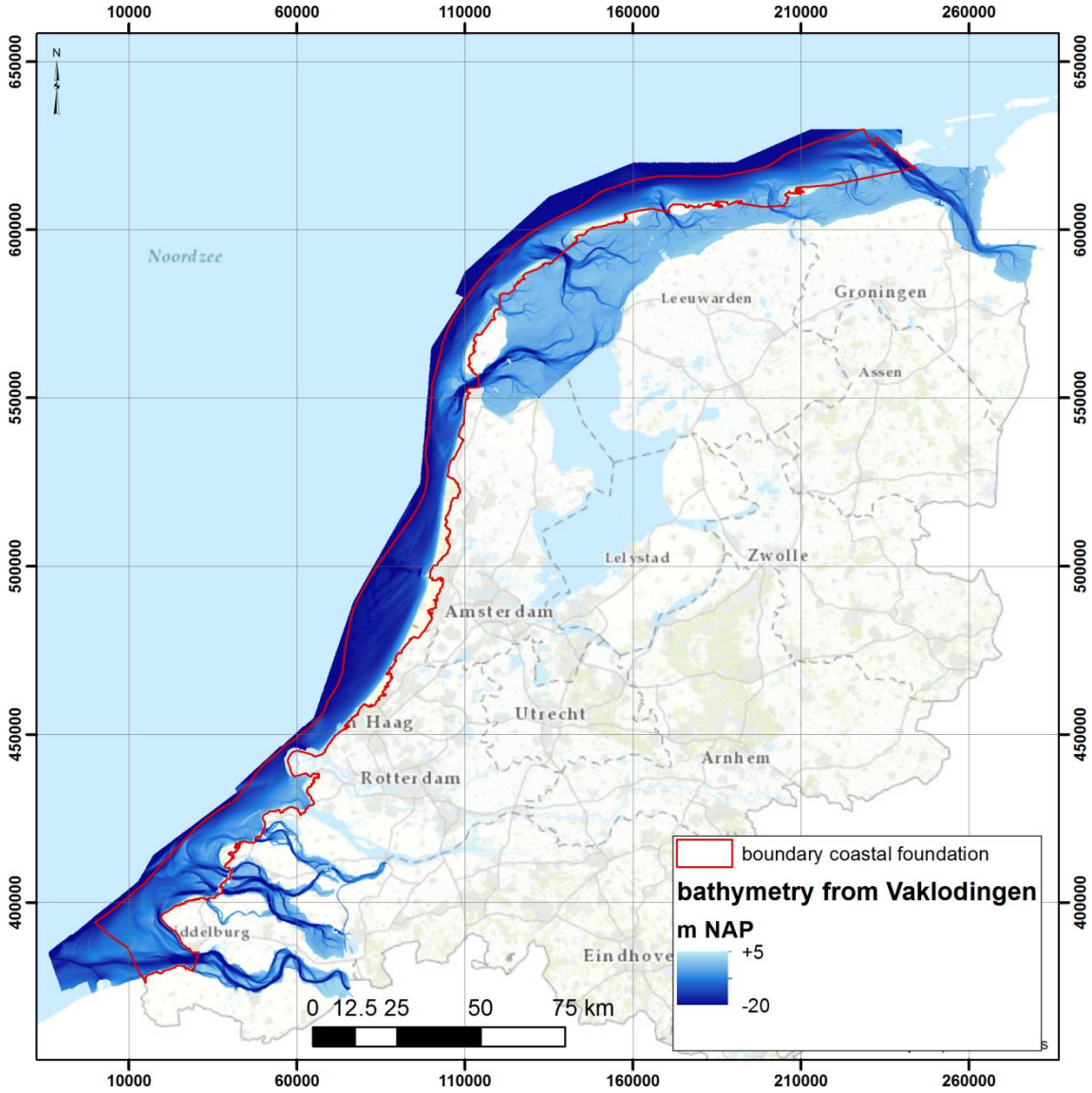

Figure 1.1 Coastal foundation on top of bathymetry from Vaklodingen between 2009 and 2014.

1.2 Objectives and research questions

This report focusses on the characteristics and temporal and spatial variability of currents and bedforms observed during the KG2 field campaigns (2017-2018). The report aims to enhance our understanding of the lower shoreface morphodynamics and, with that, contribute to the first main KG2 research question. The study builds on, and is an extension of, previous work carried out within KG2 of Leummens (2018) and Treurniet (2018), and within SEAWAD of Brakenhoff et al. (2019a) and Brakenhoff et al. (2019b).

The objective of this report is to give a detailed analysis of the spatial and temporal variability of wave-induced near-bed orbital motion, residual (non-tide driven) currents, and small-scale bedforms on the Dutch lower shoreface. The research questions are defined in the additional KG2 contract (July 2019), these are:

1. What are characteristic values for the near-bed wave orbital amplitude and net (residual) velocities on the lower shoreface of Ameland, Terschelling and Noordwijk?

2. How do the near-bed wave orbital motion and residual velocities vary with depth, wave, and wind conditions?
3. How does the observed near-bed wave orbital motion compare to a well-established parametrization (i.e., Ruessink et al., 2012)?
4. What are the characteristic bedforms found on the lower shoreface?
5. How do the bedforms vary with location, depth, and wave, tide and wind conditions?
6. How do the bedform characteristics derived from observations compare to the characteristics derived via established formulations (e.g., Van Rijn, 2007)?
7. What concepts can be derived from the analysis and do they confirm our conceptual understanding of lower shoreface morphodynamics?

1.3 Approach

The analysis in this report builds upon previous work within the KG2 project. Van der Werf et al. (2017) present a literature study on the Dutch lower shoreface. Treurniet (2018) studied the hydrodynamics at the lower shoreface of the Ameland Inlet, focussing on wave-induced orbital velocities, and Leummens (2018) focussed on residual currents. The hydrodynamic sections in this report adopt their methodology and apply it on the complete KG2 lower shoreface observational data set. The bedform sections build upon previous work performed within the SEAWAD project. The methodology and analyses described by Brakenhoff et al. (2019a) and Brakenhoff et al. (2019b) for the Ameland ebb delta are adopted here for the entire KG2 lower shoreface data set. The findings will be placed in the light of the conceptual model described by Van der Werf et al. (2017).

1.4 Outline

The KG2 measurement campaigns, instrument settings and raw data processing are described by Van der Werf et al. (2019) and are not repeated here. In the present report, Chapter 2 describes the field conditions and focusses on the methods to analyse the observed data and the theoretical background underlying the methodology. Chapter 3 describes the hydrodynamic results, presenting results on the near-bed wave orbital motion (Section 3.1) and residual currents (Section 3.2). Chapter 4 presents the results of the analysis on small-scale bedforms at the lower shoreface. Chapter 5, integrates the findings of Chapter 3 and 4 and discusses how these findings fit in the conceptual understanding of lower shoreface morphodynamics. The conclusions and recommendations are given in Chapter 6.

2 Field observations, methods, and theoretical background

2.1 Introduction

The basis for the analysis of hydrodynamics and (small-scale) bedforms at the lower shoreface are the data gathered at the frame locations within the KG2 lower shoreface campaigns (Figure 2.1; DVA, DVT1, DVT2, DVN). The observations of the Amelander Inlet campaign (AZG) are, however, included, in the sections on bedforms because they highlight the difference between these two types of field sites. The field observations used are: the water depth, derived from pressure transducers (PT); flow velocities near the bottom, measured with an Acoustic Doppler Velocimeter (ADV); flow velocity profiles from Acoustic Doppler Current Profilers (ADCP); and high-resolution Digital Elevation Models (DEM) from the sea bed directly below the frame, gathered with a 3D Sonar Ripple Profiling Logging Sensor (3DSRPLS, or simply SONAR). An overview of the field campaigns, frames, time period of operation, and available instruments is given in Table 2.1. All data used are available in NetCDF format via the KG2 data repository[1]. Descriptions of the measurement campaigns, instrument calibration, raw data-processing, and data quality checks are given in the KG2 data report (Werf et al., 2019). The methodology that is followed to analyse the data is described in the following paragraphs.

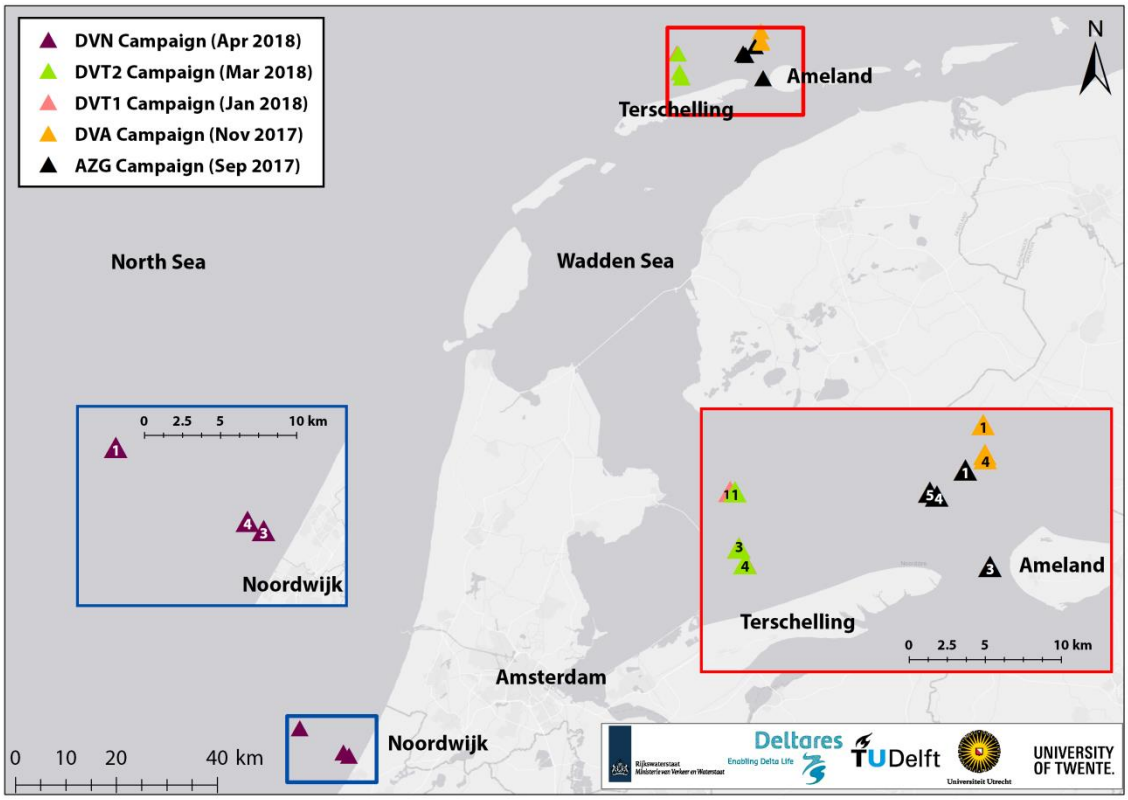

Figure 2.1 Locations of the frames of all KG2 field campaigns.

[1] https://kustgenese2.deltares.nl/

Table 2.1 Overview of KG2 measurement campaigns, frames and available instruments (shaded green).

Campaign	Code	Frame	(RDx, RDy)	Depth	Period		Instruments		
			(m)	(mNAP)	Start	End	ADV (inc.PT)	ADCP (inc.PT)	SO-NAR
Ameland lower shoreface	DVA	F1	(168339,615736)	-20	8 Nov 2017	11 Dec 2017			
		F3	(168449,613779)	-16					
		F4	(168472,613485)	-10					
Terschelling lower shoreface	DVT1	F1	(151671,611326)	-20	11 Jan 2018	6 Feb 2018			
		F3	(152260,607627)	-14					
		F4	(152685,606596)	-10					
Terschelling lower shoreface	DVT2	F1	(151993,611306)	-20	12 Mar 2018	26 Mar 2018			
		F3	(152249,607599)	-14					
		F4	(152662,606583)	-10					
Noordwijk lower shoreface	DVN	F1	(76940,477601)	-20	4 Apr 2018	15 May 2018			
		F3	(86695,472149)	-12					
		F4	(85613,472749)	-16					
Amelander Inlet (used only for bedform analysis)	AZG	F1	(167169,612748)	-8	30 Aug 2017	9 Oct 2017			
		F3	(168783, 606398)	-20					
		F4	(165276, 611043)	-5					
		F5	(164817, 611279)	-4					

Besides the data gathered within the KG2 campaigns, additional data were gathered for the analysis. These include:

- Measured meteorological data from KNMI stations Hoorn Terschelling and Wijk aan Zee, available via the KG2 repository as well;
- Modelled surface wave characteristics (H_s, T_p, wave direction) at the frame locations using the wave transformation table which was validated for the Dutch lower shoreface (Grasmeijer, 2018; Grasmeijer et al., 2019).

2.2 Field conditions

2.2.1 Tidal conditions

The Dutch coast is characterized by a semi-diurnal tide where the principal lunar tidal component M_2 is the dominant frequency. The mean tidal range is at Vlissingen 3.8 m and decreases to 1.4 m at Den Helder, after which it increases again towards the east (2.2 m at Schiermonnikoog; Van der Werf et al., 2017). To present the variation in tide-driven flow at the lower shoreface the M_2 component is derived by harmonic analysis (Pawlowicz et al., 2002) on the depth averaged (ADCP) velocity data, and visualized as tidal ellipses and amplitudes (Figure 2.2). The figure shows that the orientation of the ellipse roughly follows the orientation of the coastline and is thus mainly alongshore oriented. The figure shows a NE-SW oriented ellipse at Noordwijk (DVN) and an E-W oriented ellipse at the Wadden coast (DVA, DVT1, DVT2). Furthermore, it can be seen that the amplitude increases along the coast in north-easterly direction, and decreases with decreasing water depth. The shape of the tidal ellipse varies most between an open versus a closed coastal system: at a tidal inlet (DVA) the shape of the ellipse is more circular than the elongated ellipses at the other locations. This is the result of the in- and outflow through the inlet resulting in a stronger relative importance of the cross-shore component (Van der Werf et al., 2017).

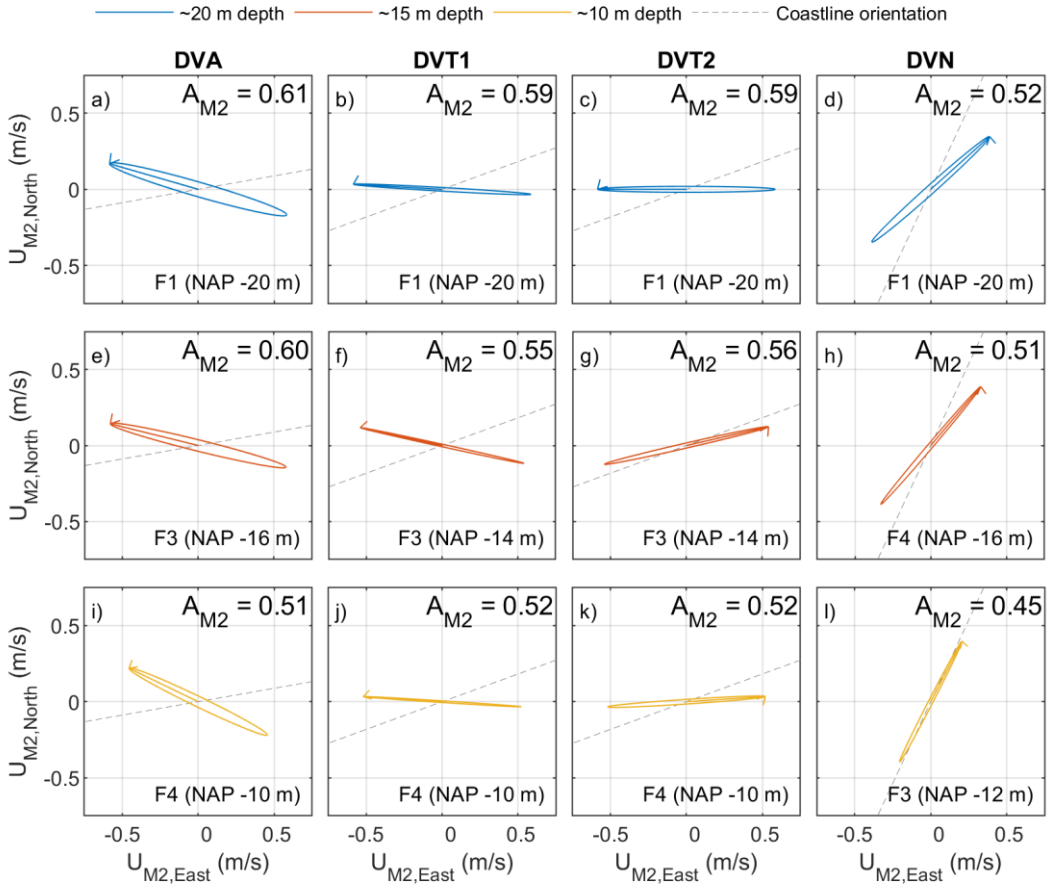

Figure 2.2 Ellipses of the M_2 tidal component derived by tidal analysis on the observed depth averaged currents.

2.2.2 Wind and wave conditions

Wind and wave conditions during the KG2 lower shoreface campaigns are shown in Figure 2.3 as directional roses based on field data (wind roses) and model results (wave roses) for the periods of the field campaigns. During the DVA campaign the most prominent wind direction was from W-SW and wind speed did generally not exceed 17.5 m/s (storm conditions are defined by wind speeds above ~17 m/s)[2]. The most prominent wave direction was from NW and with a significant wave height exceeding 4.5 m at ~20 m water depth the DVA period is characterized by quite intense wave conditions. During the DVT1 campaign wind conditions were comparable to the DVA campaign but wave conditions were milder. During the DVT2 campaign there was a very strong wind (storm conditions) blowing from ENE. The most energetic wave conditions during this campaign were from NE direction as well, with a significant wave height up to 4 m. The wind conditions during the DVN campaign were more variable than during other campaigns with prominent wind directions from NNE, ENE, and SW. Wave conditions during the DVN campaign are very mild compared to the other campaigns. This is not solely due to a change in period but a change in location as well as, in general, the Holland coast is characterized by a milder annual wave climate than the Wadden coast (Grasmeijer et al., 2019).

[2] https://www.knmi.nl/kennis-en-datacentrum/uitleg/windschaal-van-beaufort

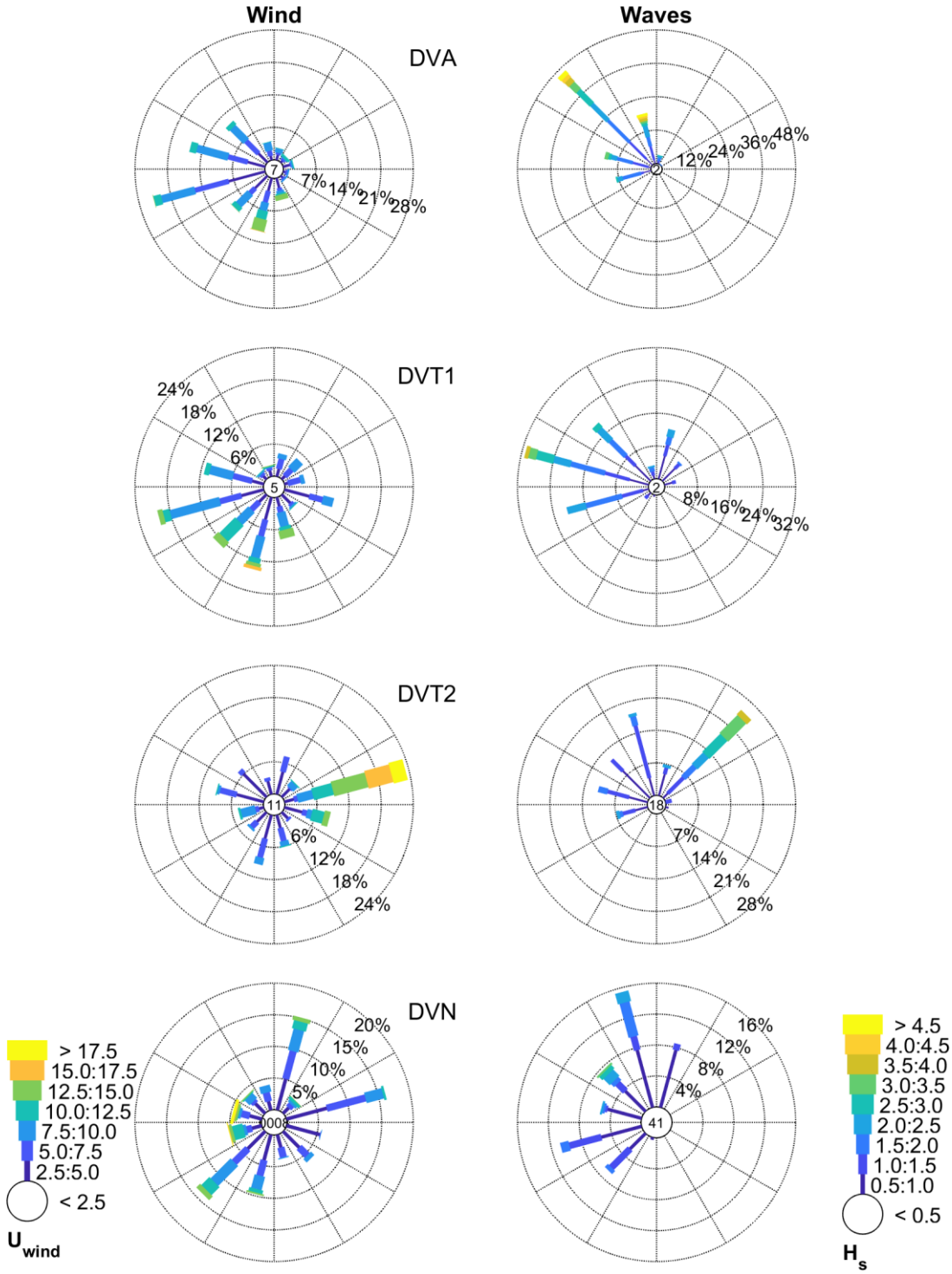

Figure 2.3 Wind (left column) and wave (right column) roses indicating the conditions during the KG2 lower shoreface field campaigns. Wind roses are based on field observations from KNMI stations Hoorn Terschelling (DVA and DVT1&2) and IJmuiden (DVN). Wave roses are based on modelled wave conditions at the most offshore KG2 frame (F1) for each campaign. Numbers in the centre circle of the roses represent the percentage of occurrences in the lowest class. Directions are given in nautical convention: coming from the given direction, measured clockwise from geographic North.

2.3 Hydrodynamics

The hydrodynamics at the lower shoreface can be subdivided into tide-induced currents, residual currents (wind,- density and wave-driven), and a wave-induced orbital motion (Van der Werf et al., 2017). Tidal currents along the Dutch coast were analysed by Zijl et al (2018). Here we will focus on the spatial and temporal variability of the wave-induced orbital motion and residual currents. Because these are closely related to the surface wave characteristics and water depth, a description on the derivation of these parameters is given first.

2.3.1 Free surface elevation

Water depth (h), significant wave height (H_{m0}) and spectral wave period ($T_{m-1,0}$) were derived from pressure sensors that were incorporated in the ADV and ADCP instruments. Pressure was converted to water depth using:

$$h = \frac{p}{\rho g} \quad (1)$$

where h is the water depth (in m), g is the gravitational acceleration (9.81 m/s^2), and ρ is the density of sea water (1023 kg/m^3). The water depth h is given by the 30-minute average. The surface wave characteristics (H_{m0} and $T_{m-1,0}$) were calculated by computing a power spectrum on 30 minutes of data of sea surface elevation (converted using a correction factor following linear wave theory). The spectral moment was calculated following:

$$m_n = \int_0^\infty f^n S_p(f) df \quad (2)$$

Here, f^n is the frequency of the oscillation of water surface elevation and S_p is the variance density for a specific frequency. The spectrum was divided in low frequencies (0.005 – 0.05 Hz) and high frequencies (0.05 – 1 Hz). The significant wave height of the sea/swell waves was calculated from the spectral moment of the high frequencies ($m_{0,HF}$) using:

$$H_s = 4\sqrt{m_{0,HF}} \quad (3)$$

For the location DVN Frame 1, wave heights and periods were derived via an alternative method. The processing was, at first, done via the ADCP pressure data. It was, however, found that the combination of the large depth and the small wave height made the derived wave heights unreliable. Therefore, the wave transformation matrix was used (Grasmeijer et al., 2019), in which offshore measured wave height and period were transformed to the nearshore locations of the frames. The wave height is the spectral wave height H_{m0}, which was also calculated for the other frames, but the wave period in the transformation matrix is given by the peak wave period T_p. T_p was converted to $T_{m-1,0}$ by dividing it by a factor 1.1, assuming a JONSWAP spectrum[3].

2.3.2 Orbital velocities

2.3.2.1 Background

Description of wave shape

In deep water, ocean waves have a, more-or-less, sinusoidal shape. As waves propagate to nearshore, they start to 'feel' the bed and their surface form becomes increasingly non-linear.

[3] https://www.helpdeskwater.nl/onderwerpen/waterveiligheid/primaire/technische-leidraden/zoeken-technische/@192915/omrekening/

First this translates into asymmetry about the horizontal axis, with short period crests and longer period throughs. This type of asymmetry is called skewness. As waves propagate further nearshore, from the shoaling zone in to surf zone, the surface form changes in asymmetry about the vertical axis (Ruessink et al., 2012). This surface form, with a steep front face and a gentle rear face, is referred to as wave asymmetry. Examples of a sinusoidal, a skewed, and an asymmetric wave are shown in Figure 2.4.

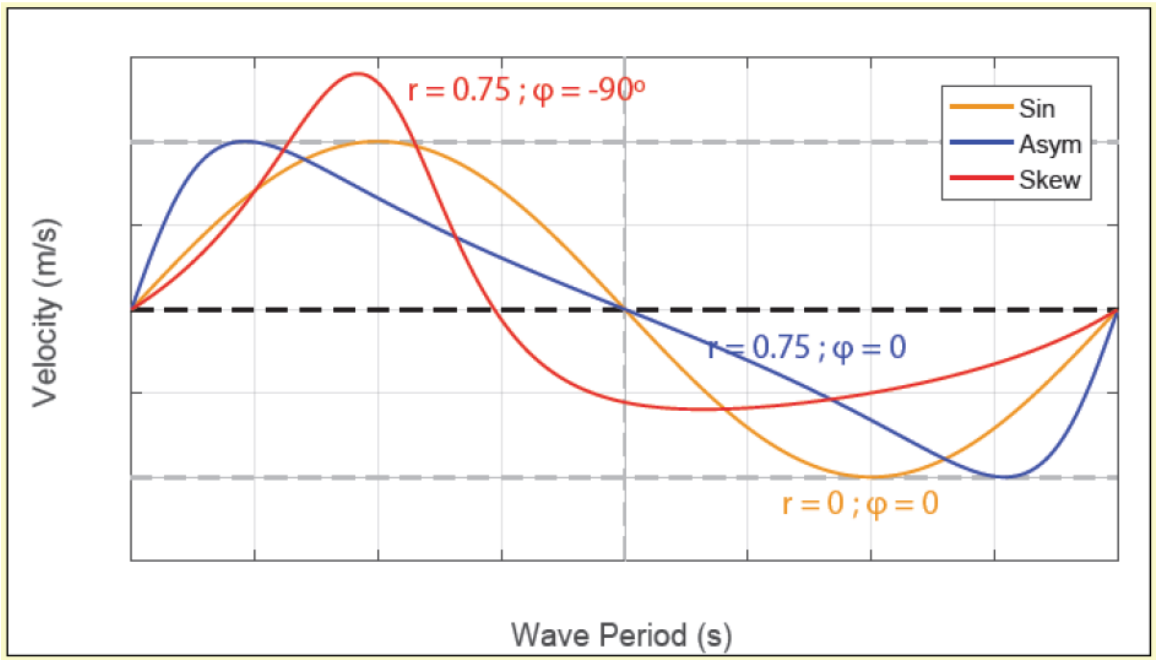

Figure 2.4 Shape of a perfectly sinusoidal, a skewed, and an asymmetric wave (from: Treurniet, 2018). The definition of the non-linearity parameter (r) and phase (φ) are given by Abreu et al. (2010).

The change towards a non-linear surface wave form is accompanied by an asymmetric wave form of the wave-induced orbital velocity profile. This can be quantified using the orbital velocity in the principle direction of wave propagation. Quantifying skewness with the skewness parameter (R_u) is given by (e.g., Ribberink & Al-Salem, 1994),

$$R_u = \frac{u_{on,\max}}{u_{on,\max} - u_{off,\max}} \quad (4)$$

where $u_{on,max}$ and $u_{off,max}$ are the maximum positive 'onshore' and negative 'offshore' orbital velocities. Skewed wave have R_u larger than 0.5, and skewness typically increases in the shoaling zone, and decreases when waves start to break in the surf zone. Wave asymmetry about the vertical axis is related to the wave orbital acceleration (R_a, derivative of u) and is quantified by (Watanabe and Sato, 2005):

$$R_a = \frac{a_{on,\max}}{a_{on,\max} - a_{off,\max}} \quad (5)$$

where $a_{on,max}$ and $a_{off,max}$ are the maximum positive 'onshore' and negative 'offshore' orbital accelerations. An asymmetric wave is described by $R_a > 0.5$.

The skewness and asymmetry of waves determines the direction of the net velocity and acceleration under waves and hence the direction of net sediment transport. That is; skewed and asymmetric waves generally result in onshore sand transport (Ruessink et al., 2012). Therefore, an accurate description of the near-bed orbital motion is crucial to estimate sand transport rates and direction. Abreu et al. (2010) introduced an analytical expression for the wave-induced near-bed orbital motion,

$$u(t) = u_w f \left(\frac{\sin(\omega t) + \frac{r \sin\phi}{1+\sqrt{1-r^2}}}{1 - r\cos(\omega t + \phi)} \right) \quad (6)$$

Where t is time, the angular frequency is given by $\omega = 2\pi / T$ (T is the wave period), $f = \sqrt{1-r^2}$ is a dimensionless factor, and the wave velocity amplitude is defined as:

$$u_w = (u_{on,\max} - u_{off,\max}) / 2 \quad (7)$$

The parameter *r* is a measure of the non-linearity and ϕ is the phase. Defining skewness and asymmetry with (4) and (5), respectively, results in a monochromatic form of the wave-induced near-bed orbital motion (equation (6)). Therefore, it describes the intra-wave velocity profile for regular waves rather well but was found to compare poorly to a series of natural random (irregular) waves. Ruessink et al. (2012) proposed a new methodology to compute the non-linearity parameter (r) and phase (φ) from the representative surface wave parameters and water depth, such that the wave form (skewness and asymmetry) described by equation (6) is representative for a series of natural random waves. For this method they defined the skewness as:

$$S_u = \frac{\overline{u_w^3(t)}}{\sigma_w^3} \quad (8)$$

Where σ_w is the standard deviation of $u_w(t)$. The wave asymmetry is given by:

$$A_u = \frac{\overline{\mathbb{H}u_w^3(t)}}{\sigma_w^3} \quad (9)$$

Where $\mathbb{H}u_w(t)$ is the Hilbert transform of $u_w(t)$.

In this study wave skewness and asymmetry are defined by equations (8) and (9) because they are better applicable for irregular waves.

Parametrizations of the wave orbital motion

Calculating the near-bed wave orbital velocity in the near shore zone requires wave form parameters (wave orbital velocity amplitude, skewness, and asymmetry) that are generally not known. The simplest approach to derive the near-bed wave orbital velocity amplitude is via linear wave theory,

$$u_w = \frac{\pi H_{m0}}{T_p \sinh(kh)} \quad (10)$$

Where u_w is the significant near-bed orbital velocity, k is the wave number which can be found by solving the dispersion relation (in this study the wave number is approximated using the method of Guo (2002)). Deriving the wave-induced near-bed velocity profile via linear wave theory, however, implies a sinusoidal wave and does not take skewness or asymmetry in to account. The parametrizations proposed by Isobe & Horikawa (1982) and Ruessink et al. (2012) describe the intra-wave velocity profile taking wave skewness and asymmetry into account. This makes the approaches more suitable for shallow water conditions where waves become skewed and asymmetric. Both the parametrizations require input of generally known wave characteristics (H_s, T_p, and water depth). For the mathematical representation of the parametrizations reference is made to the respective literature and for a comparison of the parametrizations on the intra-wave velocity profile reference is made to Figure 7 in Treurniet (2018).

2.3.2.2 Field observations and data-processing

Wave orbital velocities on the lower shoreface are calculated from the high frequency (16 Hz) ADV observations. At each ADV frame (indicated in Table 2.1) two ADV instruments measured velocities in the volume located at approximately ~19 cm and ~49 cm above the bed, respectively. The data from the lowest positioned ADV instrument are often interrupted, resulting in large 'data gaps', which is probably attributed to sedimentation under the instrument. Therefore the analyses in this report are focussed on the higher positioned ADV instruments, which provide velocity measurements at ~49 cm above the bed.

The basis is the ADV data stored on the Kustgenese 2.0 repository (despiked, noise remove and rotated in East, North, Up (ENU) reference plane), as described by Van der Werf et al. (2019). We processed the data by determining the wave orbital velocity signal in the direction of principal wave advance, following largely the method described by Ruessink et al. (2012). The data were split in burst lengths of 28640 samples per burst (29 min and 50 s) and detrended so that the mean in each burst equals zero. A high pass Fourier filter was applied to filter out waves with a frequency smaller than 0.05 Hz (period longer than 20 s), limiting the analysis to waves in the sea-swell frequency. The detrended and filtered velocity time series were converted to a velocity signal in the direction of principle wave propagation using eigenvector analysis. The signal was smoothed using a moving average window of 25 samples to filter out turbulence associated fluctuations and from the smoothed signal burst-averaged values of the significant orbital velocity were calculated (equation (10)). Significant peak orbital velocities are defined as the mean of 1/3 of the waves with the largest wave orbital diameter. The burst averaged values for wave skewness and asymmetry follow from equations (8) and (9).

2.3.3 Residual flow

A residual current on the lower shoreface can be forced by waves (wave breaking and near-bed streaming), wind, and spatial gradients in density (mainly due to salinity). The theoretical background of these mechanisms driving residual currents is described in the literature study on the Dutch lower shoreface (Van der Werf et al., 2017) and by Leummens (2018). For completeness, this chapter gives first a brief summary on the most important mechanisms that can drive a current at the lower shoreface before the field observations and data-processing methodology are discussed.

2.3.3.1 Background

Wave-induced currents

Wave breaking induced currents will only be important at the lower shoreface during storm conditions, when wave heights exceed a certain threshold and the surf zone is extended to the (upper part of the) lower shoreface. The energy dissipation due to wave breaking results in spatial gradients in the radiation stress, which act as a force on the water column and can lead to water level set-up, net longshore drift and an offshore directed undertow in cross-shore direction (Figure 2.5).

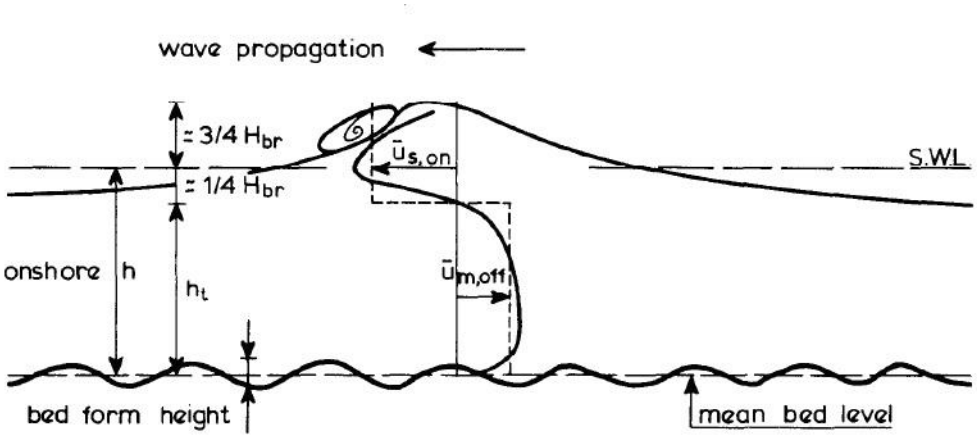

Figure 2.5 Schematized cross-shore velocity under a breaking wave (Van Rijn, 1993).

However, even in the absence of wave breaking, surface waves can generate a residual flow. Because horizontal orbital velocity increases with water depth, forward moving particles under the wave crest have a higher velocity then the backward moving particles under the wave trough. The non-closed orbital trajectories of particles under waves cause a net volume flux in the direction of wave propagation in the upper part of the profile, called Stokes drift, and can be estimated as:

$$U_s = \frac{E_w / c}{\rho h}$$

Where c is the wave celerity and E_w is the wave energy, calculated as:

$$E_w = \frac{1}{8}\rho g H_{rms}^2$$

Where $H_{rms} = H_s / \sqrt{2}$. On a closed coast, the horizontal pressure gradient that results from the Stokes drift driven water level set-up drives an offshore directed (return) current in the lower (near-bed) part of the profile, called undertow (Figure 2.6).

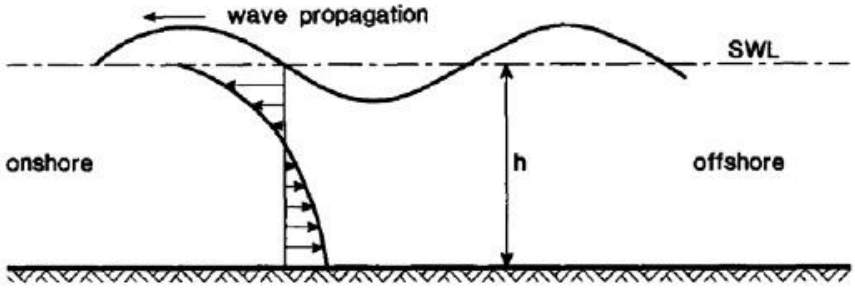

Figure 2.6 Schematized cross-shore velocity profile resulting from Stokes drift (Van Rijn, 1993).

In the very bottom part of the velocity profile (in the vicinity of the bed) a wave-induced current (near-bed streaming) results from the fact that the horizontal and vertical orbital motions are not exactly out-of-phase in the bottom boundary layer. This out-of-phase state leads to a time-averaged net downward transfer of momentum driving a boundary layer current in the direction of wave propagation (Longuet-Higgins streaming, Figure 2.7). This onshore near-bed velocity is competed by an offshore directed mean flow that results from the nonlinearity of the wave shape (velocity skewness, see Section 2.3.2.1).

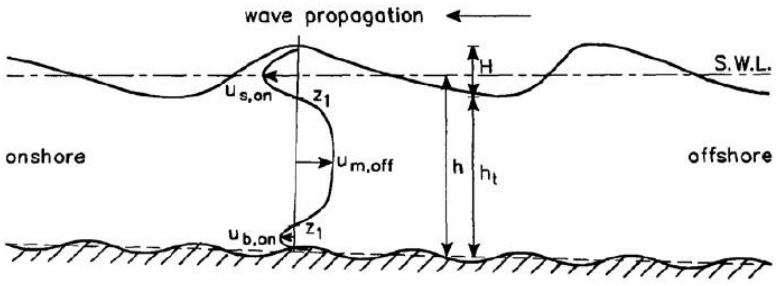

Figure 2.7 Schematized cross-shore velocity profile according to Longuet-Higgins (Van Rijn, 1993).

Wind-induced currents

In shallow water, the wind-induced shear stress on the water surface causes the upper layers of the water body to move in the same direction at the surface wind stress. The longshore component of the wind causes a net flow in the same longshore direction. The shore-normal component, however, causes a wind-induced set-up or set-down, developing a cross-shore pressure gradient. The result is an offshore (downwelling) or onshore (upwelling) current in the lower part of the velocity profile (Figure 2.8). At deeper water (larger than ~20 m), wind-induced currents are also affected by the Coriolis force, which results in the Ekman spiral flow. This flow has a 45° clockwise (northern hemisphere) rotation with respect to the wind direction, curling down to 225° clockwise current at the bed. The Ekman spiral flow results in a (depth averaged) mass flux perpendicular to the main wind direction. For the Dutch coast this means that a typical south-westerly wind results in an onshore directed surface current and an offshore directed near-bed, which can reach up to ~0.1 m/s.

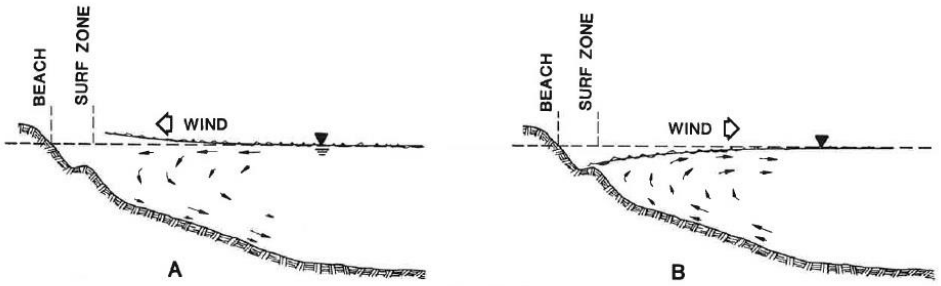

Figure 2.8 Cross-shore and vertical wind-driven current in the friction dominated nearshore zone: a) downwelling, b) upwelling (Niedoroda et al., 1985).

Density-gradient driven currents

Spatial density gradients of the fluid-sediment mixture are a result of variations in water temperature, salinity, and sediment concentrations. Nearshore gradients in salinity are the most important, which result mainly from (lower density) fresh water outflow from rivers. The onshore pressure gradient that develops due to the denser offshore water leads to an onshore near-bed current. Furthermore, the density stratification due to river outflow strengthens the tidal ellipticity (stronger during neap tide), resulting in an additional cross-shore current (De Boer, 2009).

2.3.3.2 *Field observations and data-processing*

Flow velocity profiles at the lower shoreface were measured using an ADCP. The data were processed in to 10-minute time averaged data and stored in an East, North, Up (ENU) reference plane on the Kustgenese 2.0 repository (Werf et al., 2019). Depth averaged values of the velocity profiles are available on the repository as well, derived via three methods of depth averaging. Throughout this report all the depth averaged data shown are the values that followed from a logarithmic fit to the measured data.

For the analyses, the velocity data is rotated from an ENU reference plane to its longshore and cross-shore components. The rotation follows from (Boxel et al., 2004):

$$U_{longshore} = U_{east}\cos\theta + U_{north}\sin\theta \tag{11}$$

$$U_{cross-shore} = -U_{east}\sin\theta + U_{north}\cos\theta \tag{12}$$

where $U_{longshore}$ and $U_{cross-shore}$ are velocity magnitudes in longshore and cross-shore direction, respectively, and U_{east} and U_{north} are velocity magnitudes in Eastern and Northern direction (as stored on the KG2 repository), respectively. Parameter θ is the angle of the coastline (where 0° is East), so the orientation of the coastline needs to be known. The value that is chosen for the orientation of the coastline, however, has an effect on the calculated longshore and cross-shore magnitudes (Grasmeijer et al., 2019) and should therefore be consistent between locations. In this study the orientation was simply determined via visual estimation and taken equal for all frames within a field campaign. The values chosen for the coastline orientation are indicated in Table 2.2.

Residual currents were determined by filtering out the tidal variations. Leummens (2018) analysed methods to filter out tidal variations for this dataset specifically and found low-pass filtering in the frequency domain using a Fourier transform to give the best results, mainly due to a sharp transition from stopband to passband and a limited loss of data at both sides of the

time series. Leummens (2018) defined a transition from stop frequency (30 hrs) to pass frequency (40 hrs) using a cosine taper to avoid ringing through the entire dataset. Applying a cut-off frequency of 30 hrs (0.033 cycles p/h) resulted in a complete removal from diurnal and semi-diurnal tidal variation from the timeseries of approximately one-month length. Therefore, this method was adopted for this study.

The results of residual flow velocity profiles (Section 3.2.2) are shown for storm and fair-weather conditions. The subdivision of these conditions is based on wave conditions at the deepest frame of the campaigns and the magnitude of depth averaged residual flow (Section 3.3.1). The definition of storm and fair-weather periods are indicated in Table 2.2 for each KG2 campaign.

Table 2.2 Coastline orientation (in degrees, clockwise from geographic North) and definitions of storm and fair-weather periods for the KG2 lower shoreface campaigns.

Campaign	**Coastline orientation (°)**	**Storm period**		**Fair-weather period**	
		Start	End	Start	End
DVA	80	16 Nov 2017	21 Nov 2017	21 Nov 2017	26 Nov 2017
DVT1	70	15 Jan 2018	20 Jan 2018	20 Jan 2018	25 Jan 2018
DVT2	70	16 Mar 2018 12h	19 Mar 2018 12h	20 Mar 2018	24 Mar 2018 12h
DVN	25	23 Apr 2018	5 May 2018	10 Apr 2018	20 Apr 2018

2.4 Bedforms

2.4.1 Background

The type of bedforms depends on the wave and current conditions (e.g. Soulsby, 1997; Nielsen, 1992). If the flow is too weak to cause sediment motion, the bed topography will be dominated by relict bedforms from previous more energetic events and if no such events have occurred recently, the topography will be dominated by bioturbation. Figure 2.9 shows an example of bedform distribution from Nielsen (1992).

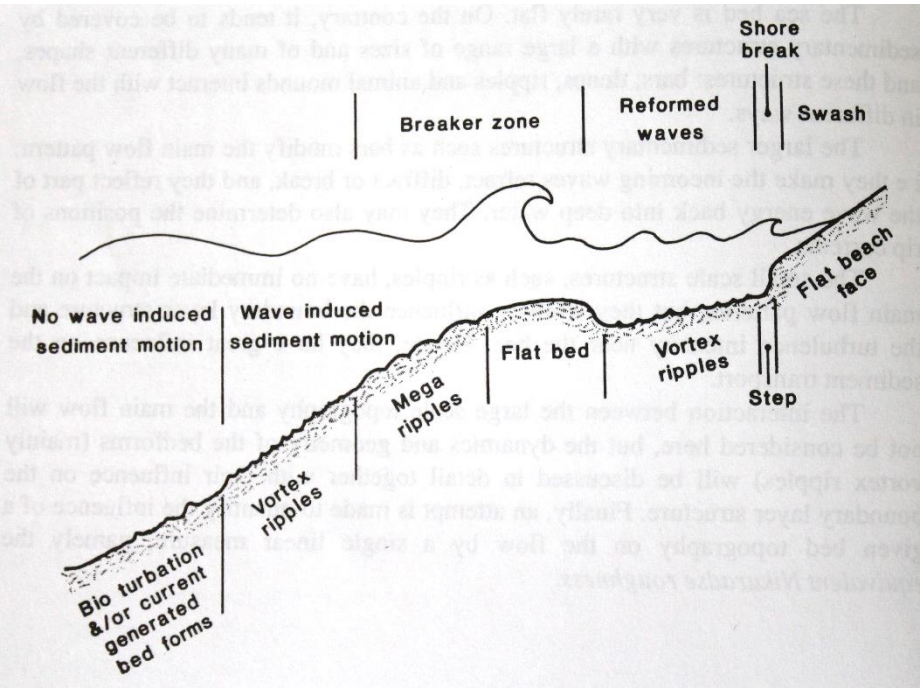

Figure 2.9 Example of bedform distribution from Nielsen (1992).

Here we repeat the knowledge about current and wave ripples that is presented by Soulsby (1997) and Nielsen (1992).

2.4.1.1 *Current ripples*

For flows that exceed the threshold of motion, an initially flat bed may deform into various types of bed features, ranging in size from small ripples up to major sand banks. Here we will focus on the ripples. These are small bed features whose height and wavelength are small compared to the water depth. They form on sandy beds with grain sizes up to about 0.8 mm, for flow speeds which are above the threshold of motion but not so intense that the ripples are washed out. At very high flow speeds (for example $\overline{U}$> 1.5 m/s for D_{50} = 0.2 mm) the ripples are washed out to leave a flat bed with a sheet flow of intense sediment transport (Soulsby, 1997). At very low flow speeds, below the threshold of motion, the bed features will retain the form they had at the time when the flow fell below the threshold value.

2.4.1.2 *Wave ripples*

Wave-generated ripples are symmetrical about the crest in cross-section, with the crest being relatively sharp. Their wavelength λ is typically between 1 and 2 times the wave orbital amplitude. Their height η is typically between 0.1 and 0.2 times their wavelength (Soulsby, 1997). Because of their sharp crestedness, there is vortex shedding from the tops.

Vortex ripples are of special interest for coastal sediment transport studies because their influence on the boundary layer structure and the sediment transport mechanisms is very strong (Nielsen, 1992). That is, over vortex ripples, the suspended sediment distribution will scale with the ripple height, while for other bedforms like megaripples and bars, the suspension distribution will scale with the flat bed boundary layer thickness which is much smaller than the height of those bedforms.

Vortex ripples are unique to the wave environment, and their scaling is closely tied to the wave motion. With respect to sedimentary structures, the most important difference between waves

and unidirectional flow is that wave flows have a well-defined horizontal scale, namely the wave orbital excursion A_w (Figure 2.10). The wave orbital excursion is defined as:

$A_w = H_{m0}/(2\sinh(kh))$ or $A_w = u_w T/2\pi$ (13)

According to Nielsen (1992), under an important range of conditions, the ripple length can be described by the following:

$\lambda = 1.33A_w \qquad \psi_w < 20$ (14)

In which wave mobility parameter ψ_w was computed as follows:

$\psi_w = \frac{u_w^2}{(s-1)gD_{50}}$, (15)

with $s = \rho_s/\rho$, ratio of densities of grain and water (for sand in fresh water $s = 1.65$). Under more vigorous conditions, the ripple length tends to be smaller than $1.33A_w$, but the details of the mechanisms which determine the ripple length in this regime are not well understood (Nielsen, 1992). Nielsen (1992) suggested the following simple formula's:

$\eta = (21\psi_w^{-1.85})A_w \qquad \psi_w > 10$ (16)

$\lambda = (2.2 - 0.345\psi_w^{0.34})A_w \qquad 2 < \psi_w < 230$ (17)

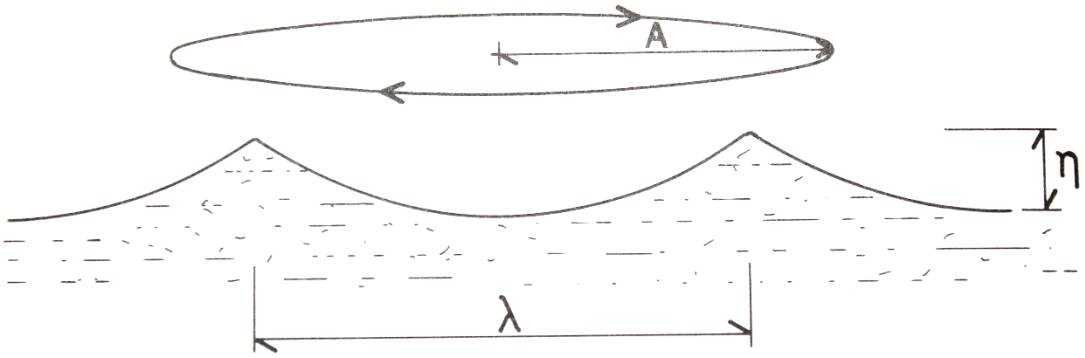

Figure 2.10. The size of vortex ripples is closely linked to the wave orbital excursion (from Nielsen, 1992)

2.4.1.3 *Hydraulic roughness of rippled beds*

According to Nielsen (1992) and Van Rijn (1993, 2007) the hydraulic roughness k_s is closely related to the ripple height. Nielsen (1992) and Van Rijn (1993) suggest the roughness to be proportional to $C\eta^2/\lambda$. The following values for *C* have been suggested: *C* = 8 (Nielsen, 1992), *C* = 16 (Raudkivi, 1988), *C* = 20 (Van Rijn, 1993), *C* = 25 (Swart, 1976), *C* = 28 (Grant & Madsen, 1984).

Nielsen (1992) suggests the following:

$k_s = 8(\eta^2/\lambda) + 170\sqrt{\theta_{2.5} - 0.05D_{50}}$

with $\theta_{2.5}$= grain roughness Shields parameter.

Van Rijn (1993) suggests the following:

$$k_s = 20\gamma_r(\eta^2/\lambda)$$

with $\gamma_r = 1$ for ripple covered bed and $\gamma_r = 0.7$ for ripples superimposed on sand waves.

2.4.2 Field observations and data-processing

The raw SONAR data were processed using the methods described by Van der Werf et al. (2019). This resulted in bed level images, showing the perturbations around the mean bed level below each SONAR at each time step. Van der Werf et al. (2019) describe two filter scales, i.e., one in which length scales smaller than 10 cm are filtered out and one in which length scales smaller than 5 cm are filtered out. Here we use the images with the length scales smaller than 5 cm filtered out because the ripples can be 5–10 cm long and because the 5 cm filtered grid is smaller and therefore less disturbed by scour and accretion around the frames' legs. Some disturbances are still visible however (Figure 2.11A). To remove these disturbances, we detrended them with a third-order surface fit, so that only the small-scale ripples remain (Figure 2.11B).

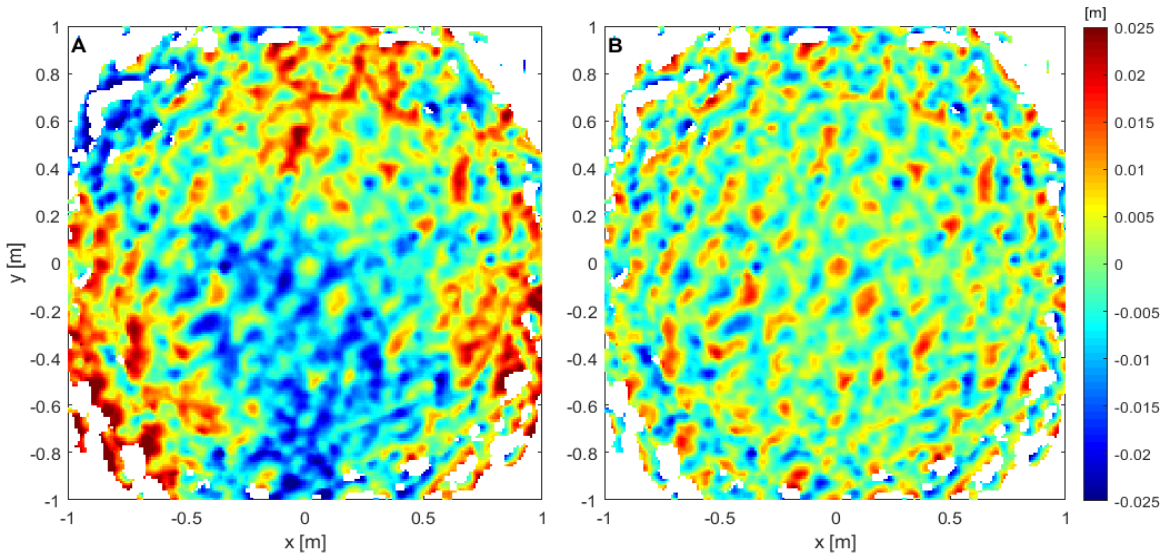

Figure 2.11 The original image (A) and the detrended image (B) of DVA, F1P1, 9 nov 2017, 20:00.

Using the detrended images, the ripple characteristics were calculated with the methods described in Brakenhoff et al. (2019), which are briefly repeated here. Ripple height η was given by $2\sqrt{2}\sigma$, with σ being the standard deviation of the detrended image. Then, each image was rotated in a full circle with steps of 5° and for each rotation the bedform three-dimensionality (Tb) was calculated using the auto-correlation of the bed elevation data in the x and y-direction according to Núñez-González et al. (2014). Tb is a dimensionless parameter, ranging from 0 (indicating a purely 2D bedform) to 1 (indicating a purely 3D bedform). The rotation angle that resulted in the lowest value of Tb was taken to be the orientation of the ripples α, although for highly three-dimensional bedforms this orientation is arbitrary. Along the main orientation, ripple lengths were calculated by a wavelet (Grinsted et al., 2004; Torrence and Compo, 1998). The wavelength with the maximum power was calculated for each grid row, and then the median of all these wavelengths was taken to be the 'dominant' ripple wavelength λ. The calculated ripple characteristics were removed if the data quality flag was -1 (described by Van der Werf et al., 2019).

To compare the ripple dimensions to the hydrodynamics, current velocities, wave heights and water depths are required. These parameters are derived from the field observations following the methods described in Section 2.3. The hydrodynamic parameter required to describe the wave-induced near-bed orbital motion (u_w) is estimated from the surface wave parameters (via linear wave theory, see Section 2.3.2) and not from the ADV observations directly. This method was preferred over the ADV observations because data gaps in the ADV time series resulted in a 25% loss of useable bedform observations. Furthermore, this permitted the analysis of the shallowest frame locations due to a complete absence of ADV instruments on these frames (see Table 2.1).

Besides hydrodynamic parameters, information on the sediment particle diameter is required. The median grain size diameter (D_{50}) were determined by box core samples and the results are given in Table 2.3 for each location where the frame was equipped with a SONAR. This table shows the mean water depth per location as well.

Table 2.3. Grain size and mean depth of all frames.

Site	Grain size (µm)	Mean depth (m)
AZG1	225	6.8
AZG3	216	16.2
AZG4	186	9.0
AZG5	186	6.5
DVA1	226	20.3
DVA3	197	16.3
DVA4	197	11.2
DVT1-1	237	19.2
DVT2-1	237	19.0
DVT2-4	197	11.6
DVN1	332	20.3

With D_{50}, $T_{m-1,0}$, H_{m0}, h, u_w and u_c, wave- and current related Shields parameters θ_w and θ_c were computed as follows:

$$\theta_w = \frac{\tau_w}{(\rho_s-\rho)gD_{50}} \quad (18)$$

$$\theta_c = \frac{\tau_c}{(\rho_s-\rho)gD_{50}} \quad (19)$$

with $\tau_w = 0.25\rho f_w u_w^2$ and $f_w = e^{\left(-6+\left(5.2A_w/(3D_{90})\right)^{-0.19}\right)}$, max($f_w$) = 0.3, $\tau_c = 0.125\rho f_c u_c^2$, $f_c = 0.24(\log(12h/D_{90}))^{-2}$, ρ_s: sand density, ρ: water density, g: acceleration due to gravity = 9.81 m/s^2.

All hydrodynamic variables were interpolated to the time vectors of the ripple data. After that, all variables, including the ripple characteristics, were saved in a mat-file per frame (Table 2.4). Each mat-file is given the name of the frame it represents (e.g., DVA1 for Diepe Vooroever Ameland Frame 1).

Table 2.4. Contents of the matfiles.

Field name	Contents
time	Date vector [yyyy mm dd HH MM SS]
eta	Ripple height [m]
lambda	Ripple wavelength [m]
Tb	Ripple three-dimensionality [-]
alpha	Orientation of the ripple crests in clockwise degrees North [º]
Hm0	Spectral wave height [m]
T	Spectral wave period [s]
h	Water depth [m]
uc	Depth-averaged current velocity [m/s]
uw	Near-bed orbital velocity [m/s]
thetaC	Current-related shields parameter [-]
thetaW	Wave-related shields parameter [-]
D50	Median grain size [m]

Using the matfiles, the hydrodynamics and bedform characteristics were compared. Also, these variables were used as input for the Van Rijn (2007) and Soulsby et al. (2012) bedform height predictors (see Appendix A for the predictor equations). The predictor of Van Rijn (2007) is incorporated in the Delft3D model. Soulsby et al. (2012) recently created a predictor in which time adaptation effects are considered.

3 Hydrodynamic results

3.1 Orbital wave characteristics

Wave-induced near-bed significant wave orbital velocity amplitude (u_w), skewness (S_k), and asymmetry (As) are derived from the ADV measurements following the approach described in Section 2.3.2. Time series of these wave orbital motion parameters are shown together with the significant wave height and relative wave height (H_s/h) (see Section 2.3.1) for all lower shoreface field campaigns (Figure 3.1 – Figure 3.4).

The time series show that near-bed orbital velocities are in the order of 0.1 m/s during mild wave conditions ($H_s \leq 0.1$ m) and are slightly larger at the shallower frame (dependent on water depth, see equation (10)). During energetic wave conditions ($H_s > 4$ m), the near-bed orbital velocity can exceed 1 m/s at the shallowest frame (~15 m water depth) and reaches a maximum of approximately 1 m/s at the deepest frame (~20 m water depth). The relative wave height does not exceed 0.3, indicating that waves are not breaking in the lower part of the lower shoreface. The skewness (S_k) fluctuates between $-0.5 < Sk < 0.5$, which agrees well with the findings of Treurniet (2018). During high energetic wave conditions ($H_s > 2$), waves become skewed, which increases with a decrease of water depth. The asymmetry of the waves does not show such a clear relation in the time series.

A comparison of the wave orbital velocity amplitude found during the field campaigns (hence, between locations and conditions) is visualized by plotting discretized values of the significant wave height with the averaged values of the accompanying u_w (Figure 3.5). The figure shows that the wave-induced near-bed orbital velocity amplitude depends linearly on the wave height (the large u_w at a small H_s of the DVA campaign at 20 m water depth is an outlier and should be ignored) and at shallower water the increase in u_w with H_s is larger than at deeper water. Furthermore, the figure shows that at Ameland (DVA) and Terschelling (DVT1 & DVT2) the observed orbital velocities scale similarly with the significant wave height. The Noordwijk (DVN) campaign shows a slightly different behaviour. It is, however, hard to draw conclusions from this observation because high energetic wave conditions were not measured during this campaign (Figure 2.3) and the shallowest frame was placed at the upper part of the lower shoreface (12 m water depth).

A comparison between the wave-induced near-bed orbital velocity amplitude (u_w) derived directly from the ADV observations and derived indirectly from the surface wave characteristics (derived from the pressure transducers) is shown in Figure 3.6. The figure shows two important features; $u_{w,measured}$ is generally larger than $u_{w,lin.\ wave\ theory}$ and the underestimation is larger at a larger water depth. The difference can be caused by a difference in the method to derive the wave orbital amplitude (see Section 2.3.2), however, a more plausible explanation is an underestimation of surface wave height (H_s) derived from the pressure transducers. The reason for this is that the dynamic pressure (due to high frequency surface fluctuations) is not captured well in the pressure signal at deep water. The increase of the underestimation at a larger water depth (Figure 3.6) supports this hypothesis.

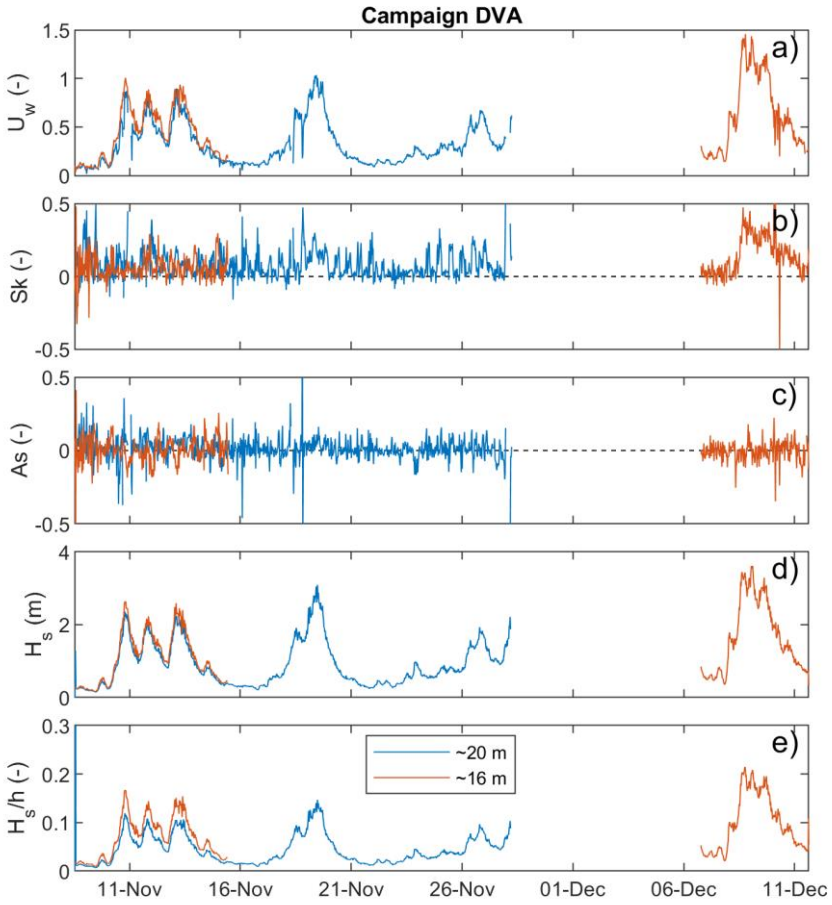

Figure 3.1 Time series of (a) the wave orbital velocity amplitude, (b) skewness, (c) asymmetry, the significant wave height (d), and the relative wave height (e) during the Ameland lower shoreface campaign in November 2017.

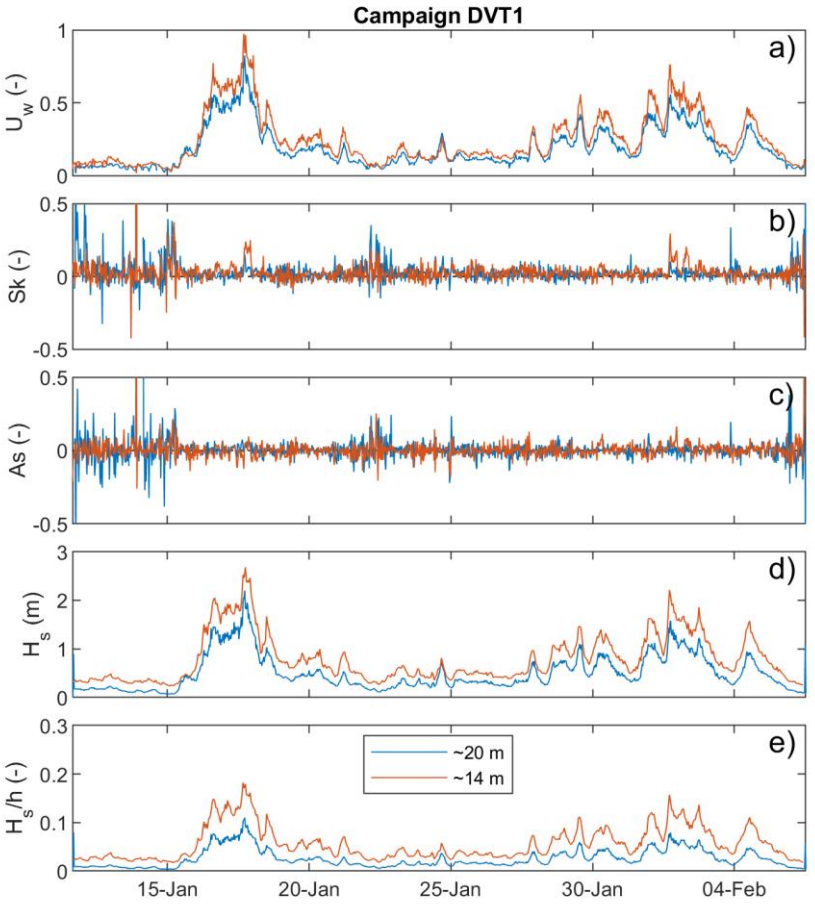

Figure 3.2 Time series of (a) the wave orbital velocity amplitude, (b) skewness, (c) asymmetry, the significant wave height (d), and the relative wave height (e) during the Terschelling lower shoreface campaign in January 2018.

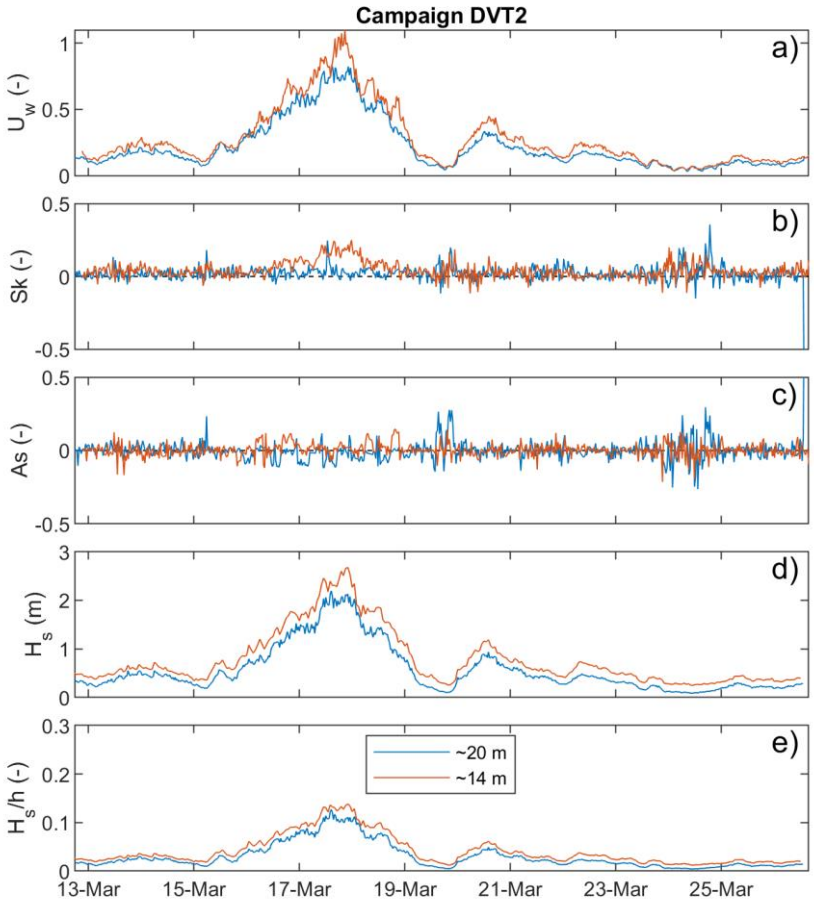

Figure 3.3 Time series of (a) the wave orbital velocity amplitude, (b) skewness, (c) asymmetry, the significant wave height (d), and the relative wave height (e) during the Terschelling lower shoreface campaign in March 2018.

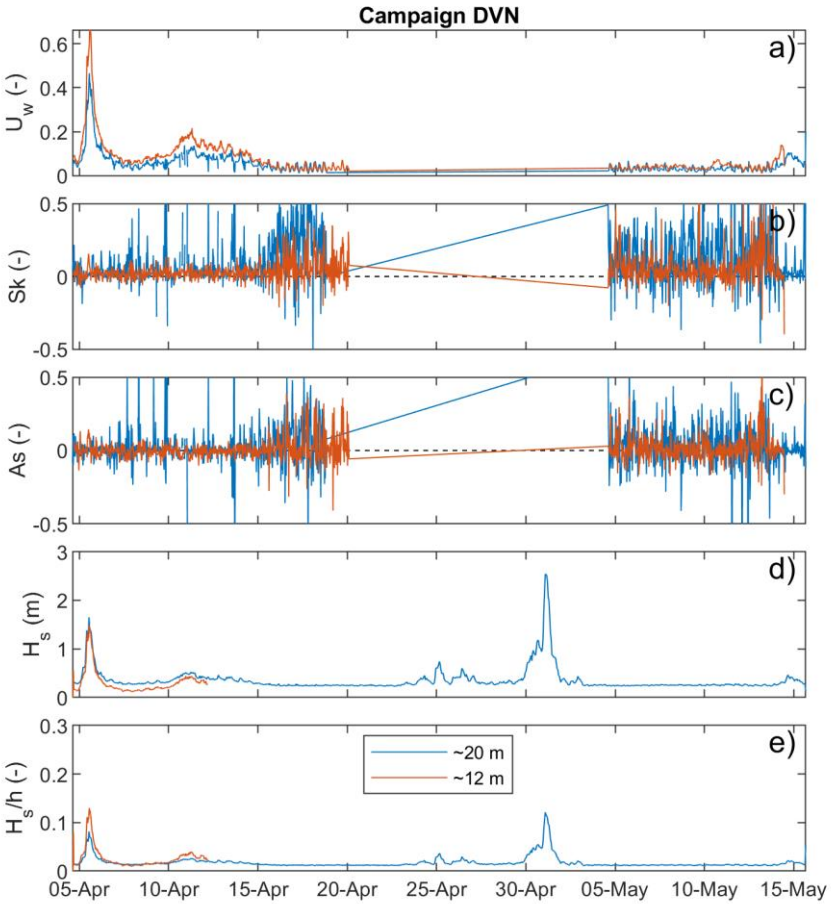

Figure 3.4 Time series of (a) the wave orbital velocity amplitude, (b) skewness, (c) asymmetry, the significant wave height (d), and the relative wave height (e) during the Noordwijk lower shoreface campaign in April 2018.

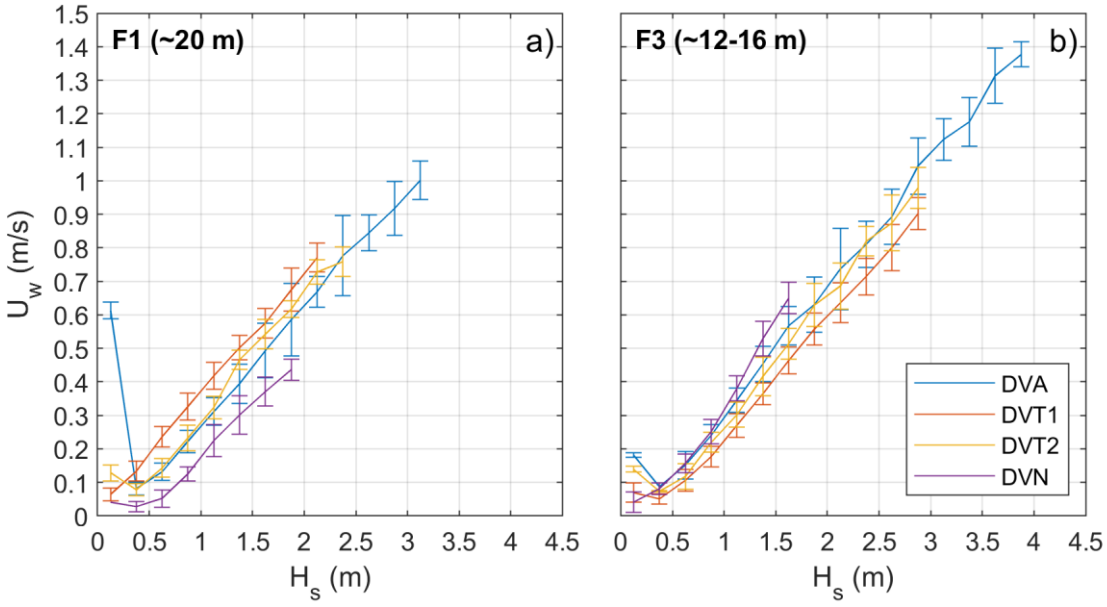

Figure 3.5 Mean significant orbital velocity amplitude (U_w) per discretized significant wave height class, for varying water depths (subfigures) and lower shoreface field campaigns (colours).

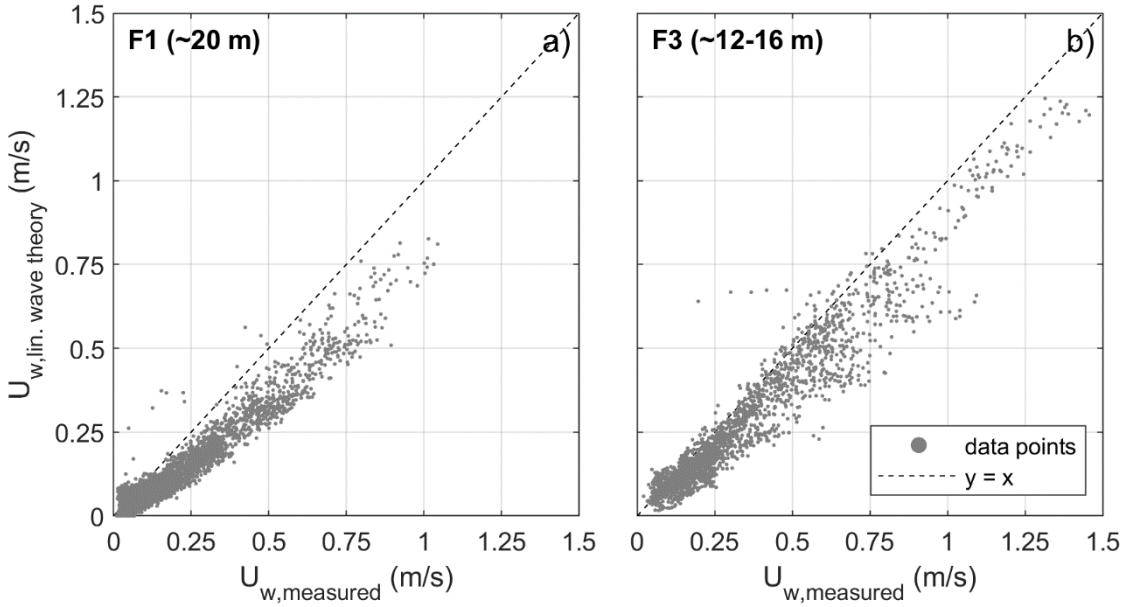

Figure 3.6 Scatterplots of the significant orbital velocity amplitude (u_w) determined by linear wave theory vs. the amplitudes derived from the ADV instruments, for ~20 m (a) and ~12-16 m (b) water depth.

To eliminate the effect of a underestimation of the surface wave characteristics in the comparison of $u_{w,measured}$ versus $u_{w,lin.\ wave\ theory}$, Figure 3.7 shows the $u_{w,measured}$ versus the wave height, accompanied by a line that gives the wave orbital velocity amplitude derived via linear wave theory with a constant water depth (h = 20 m and 15 m) and a continuous increasing significant wave height. The wave period needs to be estimated for this relation (and dependent of H_s) and is calculated as (Van Rijn, 2013):

$$T_p = 6H_s^{0.33} \quad (20)$$

This figure shows an underestimation of u_w derived via linear wave theory as well. This, however, can be attributed to a disagreement of peak wave periods derived via equation (20) and the peak wave period derived directly from the pressure transducers (Figure 3.8).

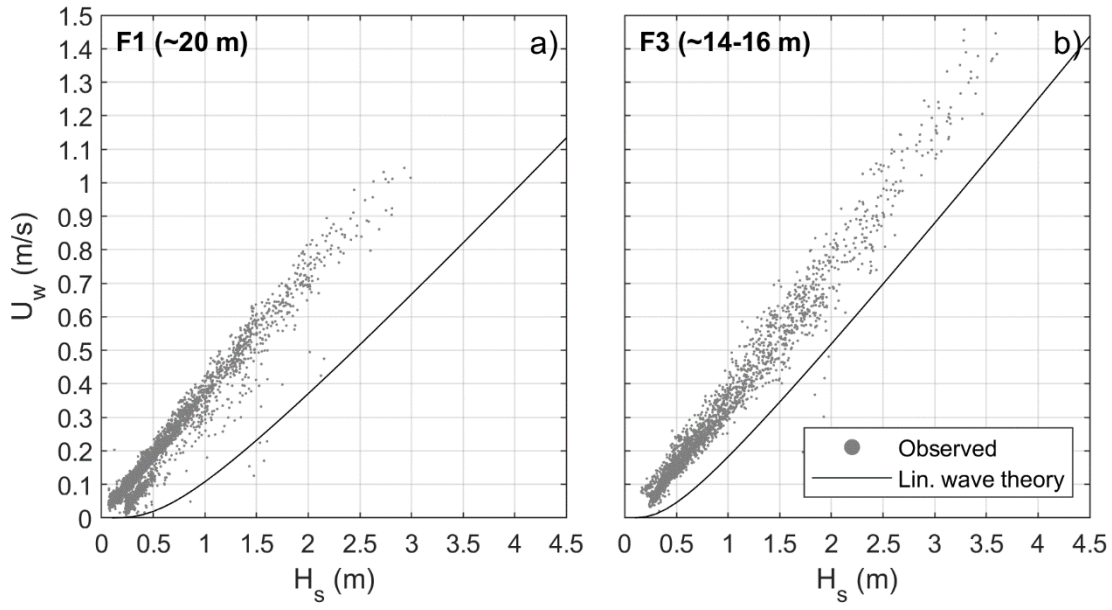

Figure 3.7 Significant orbital velocity amplitude (U_w) versus significant wave height (H_s), as measured during the field campaigns (gray dots) and estimated with linear wave theory using a constant water depth of 20 m (a) and 15 m (b).

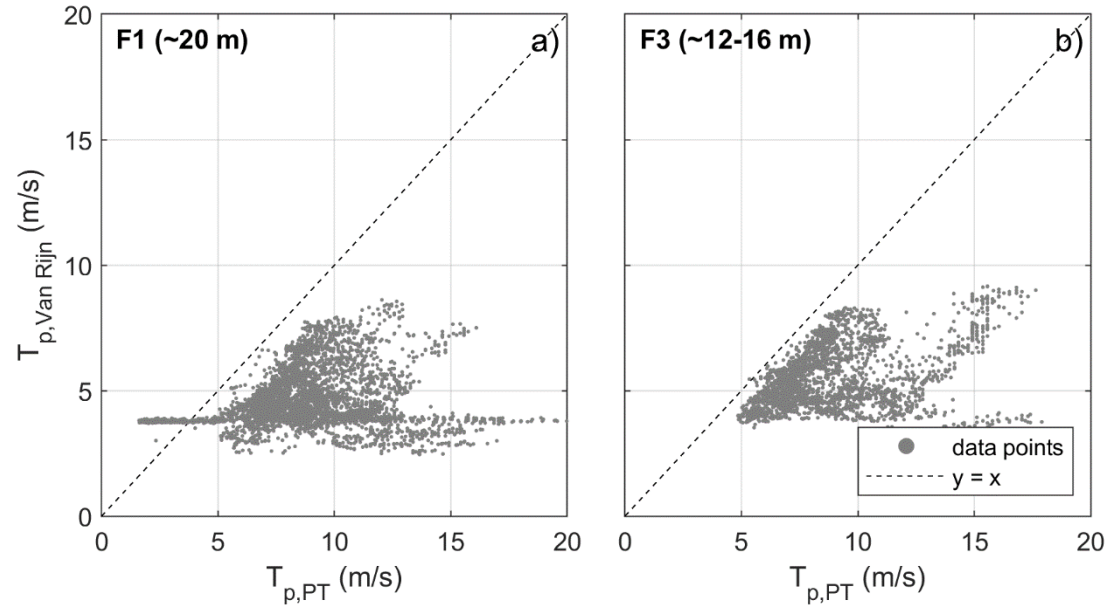

Figure 3.8 Peak wave period derived from the significant wave height following Van Rijn (1993) versus the peak wave period derived directly from the pressure transducers (PT).

The observed values for wave skewness and asymmetry are compared to the empirical relation found by Ruessink et al. (2012) (Figure 3.9). The figure shows that the wave conditions range between an Ursell nummber of $10^{-5} < Ur < 10^{0}$. This is far less non-linear than the conditions in the dataset used by Ruessink et al. (2012), which makes sense as the water depth in their dataset varied between 0.25 and 11.2 m (here, 12 – 20 m water depth). Nevertheless, the

relation defined by Ruessink et al. (2012) describes the trend in the data well. Logically, the least non-linear conditions are found at ~20 m water depth, and the most non-linear conditions at the shallower frames. From the figure can be derived that the least non-linear waves (Ur < 10^2) are not skewed and not asymmetric. However, he absolute values of *Sk* and *As* are probably slightly underestimated due to the applied moving average window of 25 samples (see Section 2.3.2). The more non-linear waves (Ur > 10^2) become skewed at the lower shoreface. Waves are not asymmetric at the lower shoreface under the conditions observed during the field campaigns.

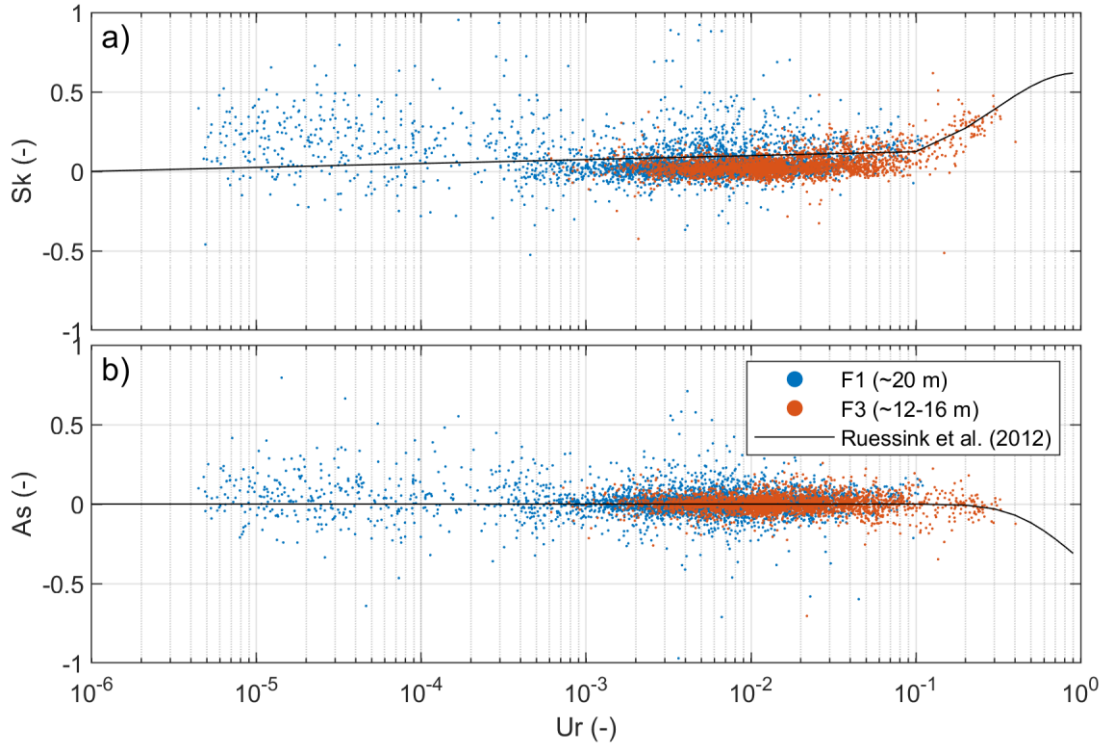

Figure 3.9 Wave skewness (a) and asymmetry (b) as observed on the lower shoreface and found with empirical relation of Ruessink et al. (2012).

3.2 Residual flow

3.2.1 Depth-averaged velocity

The magnitude and direction (cartesian convention; direction where flow vector is pointing to) of the depth averaged residual currents at the frame locations is shown for all the KG2 lower shoreface campaigns (Figure 3.10 - Figure 3.13). For each campaign the local wave conditions and the relative wave height (breaker criterium) are shown as well, determined using the wave conditions (except direction) and the water depth derived from the pressure transducer at the frame. The wind conditions from a nearby KNMI station are shown in the subplot at the bottom. Wave and wind direction are shown in nautical convention (the direction where the vector is coming from).

The residual currents at DVA were already analysed by Leummens (2018). He found that the currents at the lower shoreface are significantly altered from the tide-driven flow during storm conditions: during mild conditions there is a residual eastward longshore current and a seaward directed cross-shore current, while during energetic conditions the longshore current increases in strength and the cross-shore current is landward directed. The observations at DVA shown in Figure 3.10 do, naturally, confirm these conclusions. Additionally, the figure shows that wave breaking (Hs/H > 0.4) – although relevant for the shallowest location – is not a requirement to drive a residual current at the lower shoreface (although wave breaking can occur for the highest waves in the spectrum). The magnitude of the residual current does, however, clearly correlate to the peaks in the local significant wave height and the significance of the peaks increases with decreasing water depth, leading to an overall increase in the strength of the residual current with a decreasing water depth. It is, however, remarkable that the event with the highest local significant wave (20 November) does not necessarily drive the strongest residual current (30 Nov.). Because the longshore residual current is stronger and the cross-shore current is smaller on 30 Nov. than observed at the storm of 20 Nov., this suggests that the wave-induced residual current at the lower shoreface is not only correlated to the significant wave height.

The conditions during the two campaigns at Terschelling (DVT1 and DVT2, Figure 3.11 and Figure 3.12) are very different from each other in wind and wave direction. During DVT1 there were relatively mild wind and wave conditions coming from a north western direction, leading to a residual current strength of maximum ~0.2 m/s if the local significant wave height does not exceed ~2 m. In accordance to the findings from the DVA campaign, the strength of the current correlates with the peaks in the local significant wave height. Around 17 Jan, when the wave height exceeds 2 m, the current strength exceeds 0.3 m/s over the entire lower shoreface. In contrast to the DVA campaign the DVT1 campaigns shows that the strongest residual current is observed at the deepest location (20 m) instead of the shallowest location, which is mainly attributed to the strength of the longshore current. Only during events with increased wave heights (e.g. 17 Jan) the strength of the residual (longshore) current shows a negative correlation with water depth, similar as observed at DVA. This behaviour seems to be confirmed by the DVT2 campaign with an increasing residual current strength (up to 0.8 m/s) at shallower depths during the storm event around 18 March and a strongest current at the deepest frame during the mild conditions. However, during the very low energetic wind and wave conditions preceding and following the storm there is hardly any residual current present at the lower shoreface, leading to an insignificant difference between the three frames considered. Therefore, it is hard to confirm a negative correlation of residual current strength with water depth during mild conditions based on these observations.

A mechanism that can clearly be seen from the residual currents during the DVT2 campaign is the change of direction of the residual longshore current, which can be westward with waves and wind approaching from NE direction (15 – 19 March). Furthermore, in accordance to the high energetic wave events observed at DVA and DVT1 the cross-shore residual current during the storm of 18 March is clearly landwards and increases in strength with depth.

The conditions at DVN are milder than observed during the other three campaigns, with the local significant wave height not exceeding 1 m for most of the campaign. During the most energetic wave event (1 May, H_s > 2.5 m) the two shallowest frames did, unfortunately, not work properly but the data from the deepest frame shows a residual current up to 0.1 m/s. After this event a rotation of the residual cross-shore current can be observed from a dominantly landward to dominantly seaward directed current. This reversal of the cross-shore current direction following a storm was observed by Leummens (2018) at DVA as well. He hypothesized that, at DVA, the emptying of the Wadden Sea basin through the tidal inlet after a storm could explain this. This mechanism cannot explain the observed behaviour at DVN however.

The observations described above clearly indicate that there is a relation between the wave and wind conditions and the residual currents at the lower shoreface. An attempt to quantify these relations is shown in Figure 3.14, Figure 3.15 and in Table 3.1. Figure 3.14 shows scatterplots and linear least square regressions of the residual current strength versus the local wave energy (as a measure of the strength of Stokes drift, see Section 2.3.3). The figure shows that, in general, there is consistency between the increase in U_{res} with E_w with water depth; at shallower frames the increase in U_{res} with E_w is larger than at deeper frames. At DVT2, where there is a clear single storm event, the correlation between the wave energy and the residual current strength is strong and can be explained quite well with a linear regression (r^2 > 0.7). At the other campaigns there is quite some scatter and a linear fit does not suit the observed relationships very well.

Figure 3.15 and Table 3.1 give similar types of scatterplots and regression lines, now established for the relation between the residual current strength and wind speed. The figure and table show that at DVT2 there is the best correlation between wind speed and current strength and that the increase or U_{res} with U_{wind} becomes larger with decreasing water depth. At the other campaigns there is not a very convincing correlation (r^2 = 0).

*Table 3.1 Coefficient of the linear relationships of Figure 3.14 and Figure 3.15 of the form a*x+b, with the goodness-of-fit (r^2) given in brackets.*

	Frame	DVA	DVT1	DVT2	DVN
Waves (Figure 3.14)	F1	5.16e-06*x+0.09 (0.00)	1.00e-04*x+0.15 (0.00)	1.44e-04*x+0.04 (0.72)	1.70e-05*x+0.04 (0.00)
	F3	9.11e-06*x+0.21 (0.00)	6.57e-05*x+0.10 (0.00)	2.09e-04*x-0.00 (0.84)	3.30e-04*x+0.05 (0.00)
	F4	1.71e-05*x+0.24 (0.00)	7.86e-05*x+0.09 (0.00)	1.95e-04*x-0.01 (0.78)	6.60e-04*x+0.01 (0.81)
Wind (Figure 3.15)	F1	1.18e-02*x+0.02 (0.00)	1.27e-02*x+0.08 (0.00)	1.83e-02*x+-0.06 (0.38)	2.94e-03*x+0.03 (0.00)
	F3	2.46e-02*x+0.03 (0.00)	1.55e-02*x+0.02 (0.00)	3.64e-02*x+-0.17 (0.35)	1.13e-02*x+0.00 (0.00)
	F4	1.39e-02*x+0.17 (0.00)	1.72e-02*x+0.00 (0.00)	3.72e-02*x+-0.19 (0.39)	9.77e-04*x+0.04 (0.00)

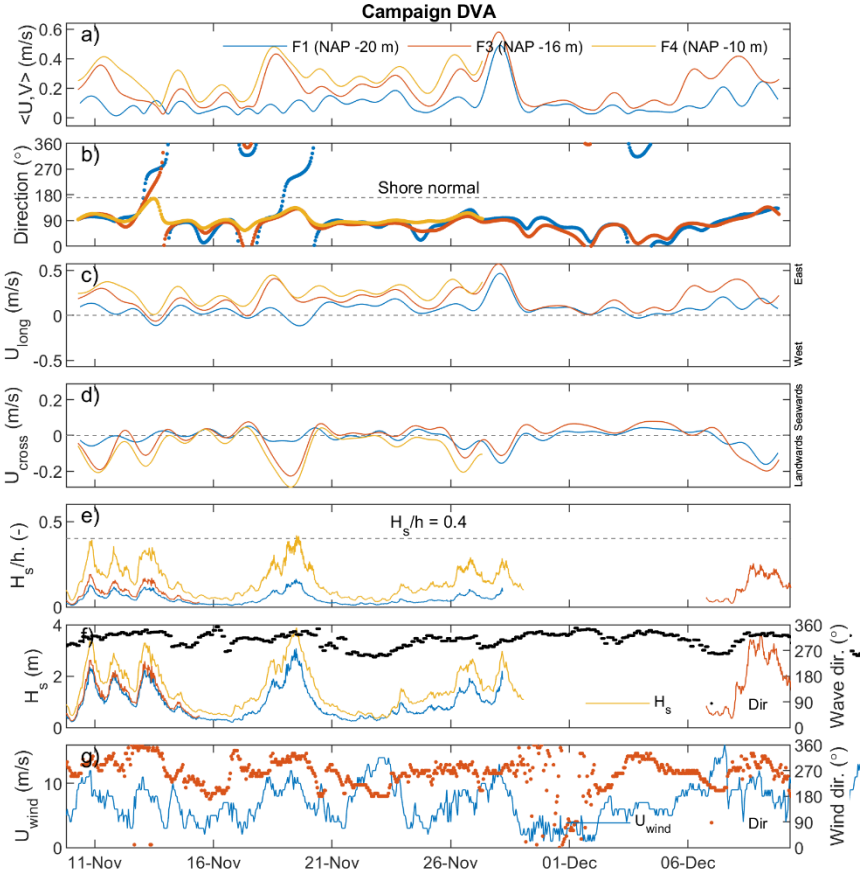

Figure 3.10 Campaign DVA: residual flow magnitude (a) and direction (b) at all frames; residual flow in longshore (c) and cross-shore (d) direction (see direction at right side of panels); breaker criterion at all frames (e); wave height (from observations) and direction (from the wave transformation matrix at the most offshore frame) (f); and measured wind velocity and direction at KNMI station Hoorn (Terschelling) (g).

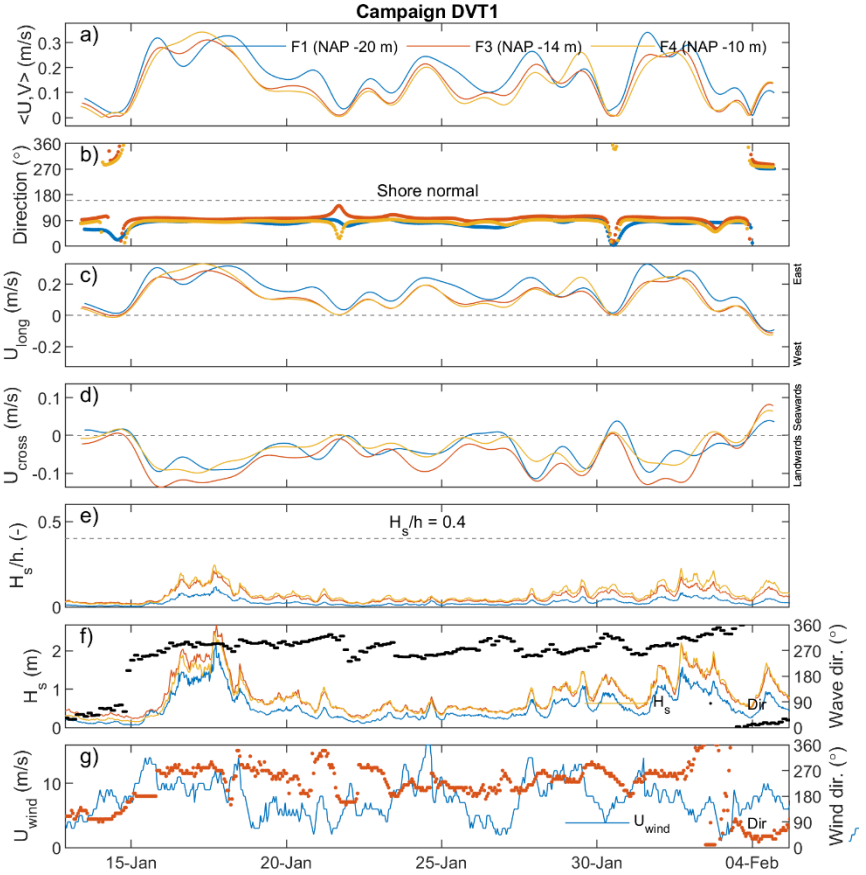

Figure 3.11 Campaign DVT1: residual flow magnitude (a) and direction (b) at all frames; residual flow in longshore (c) and cross-shore (d) direction (see direction at right side of panels); breaker criterion at all frames (e); wave height (from observations) and direction (from the wave transformation matrix at the most offshore frame) (f); and measured wind velocity and direction at KNMI station Hoorn (Terschelling) (g).

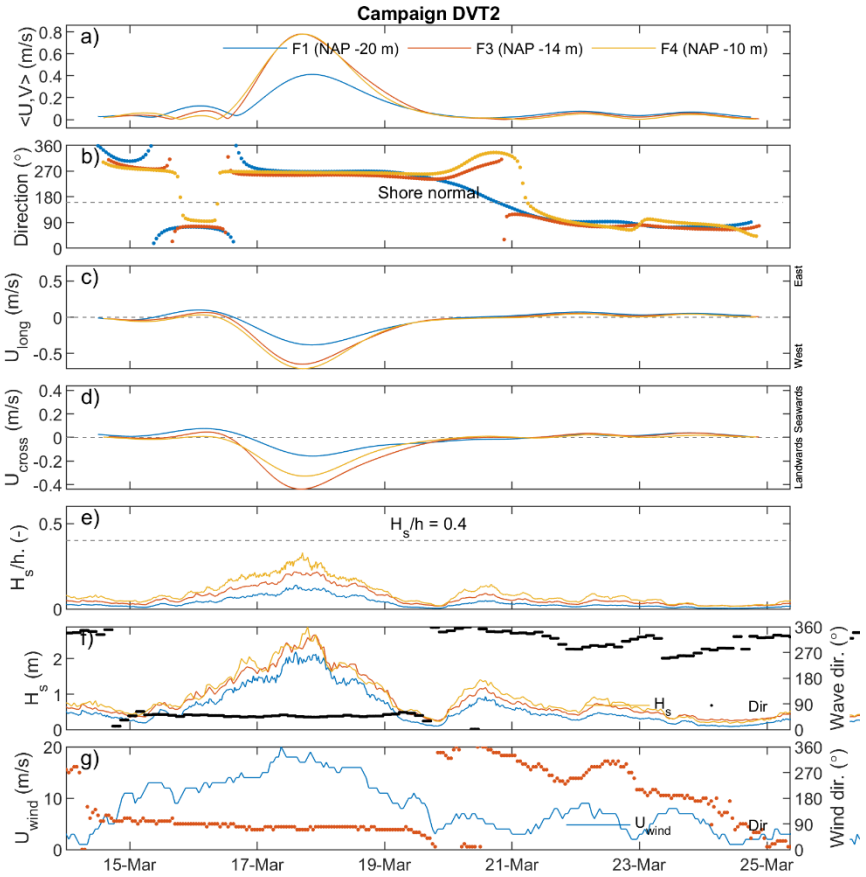

Figure 3.12 Campaign DVT2: residual flow magnitude (a) and direction (b) at all frames; residual flow in longshore (c) and cross-shore (d) direction (see direction at right side of panels); breaker criterion at all frames (e); wave height (from observations) and direction (from the wave transformation matrix at the most offshore frame) (f); and measured wind velocity and direction at KNMI station Hoorn (Terschelling) (g).

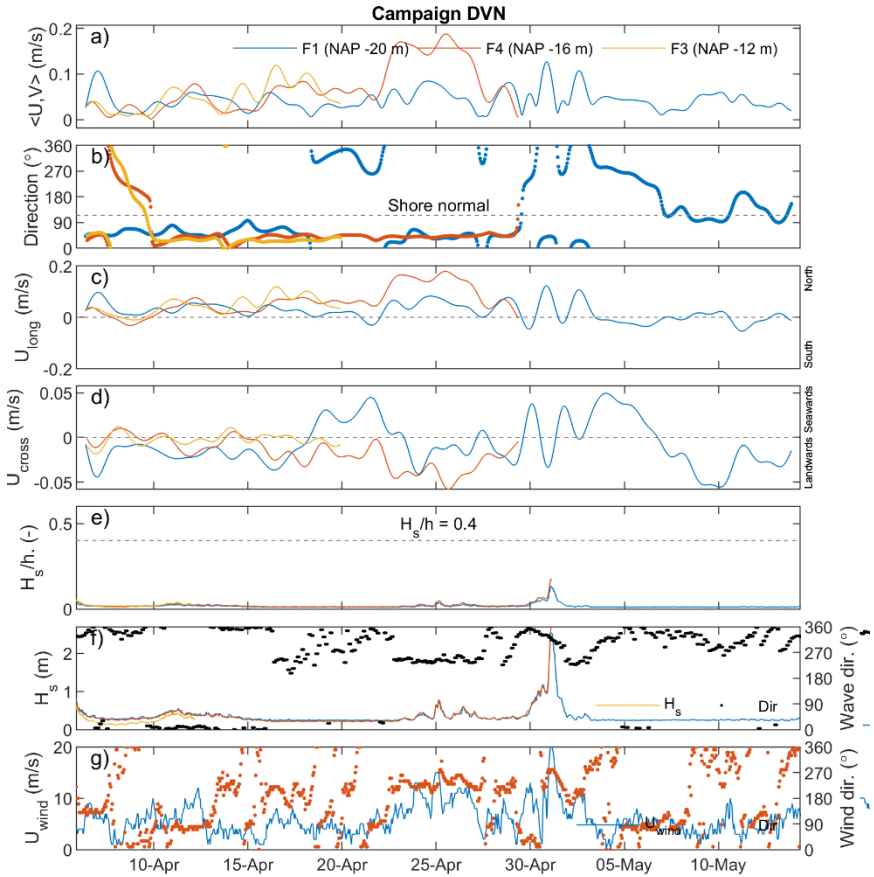

Figure 3.13 Campaign DVN: residual flow magnitude (a) and direction (b) at all frames; residual flow in longshore (c) and cross-shore (d) direction (see direction at right side of panels); breaker criterion at all frames (e); wave height (from observations) and direction (from the wave transformation matrix at the most offshore frame) (f); and measured wind velocity and direction at KNMI station IJmuiden (g).

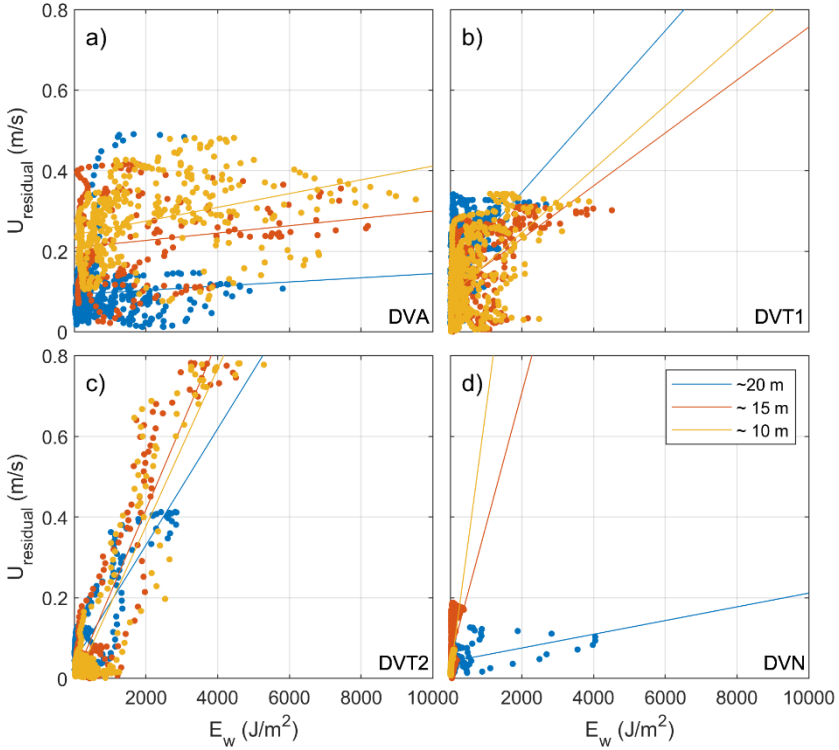

Figure 3.14 Scatterplots of the local (modelled) wave energy and residual current magnitude for different depths (colours) and locations (subplots a-d) of the Dutch lower shoreface. Lines represent linear least squares regressions on the data.

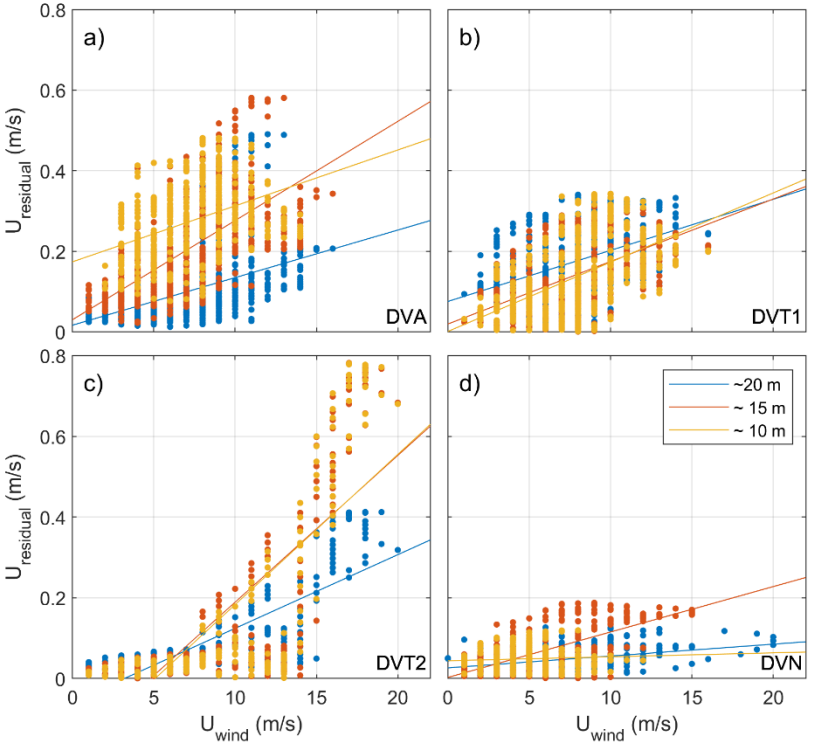

Figure 3.15 Scatterplots of the regional (nearby KNMI station) wind speed and residual current magnitude for different depths (colours) and locations (subplots a-d) of the Dutch lower shoreface. Lines represent linear least squares regressions on the data.

3.2.2 Velocity profiles

The analysis of the residual depth-averaged flow showed that there is a residual current of several decimetres per second at the lower shoreface during storm conditions. The change in lower shoreface hydrodynamics during storm conditions is studied in more detail by constructing time-averaged residual flow velocity profiles, in the longshore and cross-shore direction (Figure 3.16 and Figure 3.17) for the fair-weather and energetic conditions specified in Table 2.2. To allow comparison between different locations and water depths, the profiles are plotted as function of non-dimensional depth (z/z_{max}), where z is the height above the bed of an observation (measurement bin) and z_{max} is the total water depth. A positive or negative value in the longshore direction corresponds to a current towards the downdrift or updrift direction, respectively. In the case of DVN this is towards the North, for the other campaigns this is towards the East. The flow velocity profiles are established using solely the upward looking ADCP instruments as in most of the campaigns there are no data available for the downward looking instrument (or there was no downward looking ADCP installed). This can be seen in the figures by an absence of data in the lower part of the velocity profile and is also the reason why a distinct logarithmic velocity profile cannot always be identified from the data.

The profiles show that during fair-weather conditions the longshore velocity profile is in downdrift location over the entire depth range of the profile. The velocity maximum is near the surface and decreases towards a minimum near the bottom, although near-bottom velocity data are abscent. Moving up to shallower depths over the lower shoreface (going down in the left column of Figure 3.16) the entire velocity profile shifts to larger velocities in downdrift direction. The cross-shore velocity profile during fair-weather conditions shows a landward directed velocity in the lower parts ($z/z_{max} < \sim 0.5$) of the profile and a seawards directed current velocity in the higher part of the profile. Near the surface the direction of the profile changes towards landward direction; the effect of the landward directed flux of fluid particles in the direction of wave propagation (Stokes drift). These characteristics of the profile do not change substantially over the cross-shore direction of the lower shoreface (going down in the right column of Figure 3.16), leading to a more or less uniform flow velocity profile over the lower shoreface during fair-weather conditions.

During energetic conditions the flow velocity magnitude in the longshore direction is larger over the entire water column and the increase in longshore velocity over the cross-shore direction of the lower shoreface is enhanced with respect to fair-weather conditions. The direction of flow can change towards updrift direction if the wind and waves are approaching obliquely incident downdrift from the shore-normal, illustrated by the DVT2 campaign where the entire velocity profile is pushed in updrift direction (see also
Figure 3.12 for wind and wave conditions and Table 2.2 for periods). The cross-shore velocity profile during storm conditions changes from a depth-varying current direction during fair-weather conditions (right column Figure 3.16) towards a velocity profile that is landward directed over the entire water column (right column Figure 3.17). Exceptions can be seen on the deepest locations of DVA and DVN where the profile is similar to the profile during fair-weather conditions. At shallower frame locations the profile is changed to a profile with flow velocities in the landward direction. Apparently, there is a relation between the storm intensity and the depths on the lower shoreface where the residual cross-shore profile is altered.

•

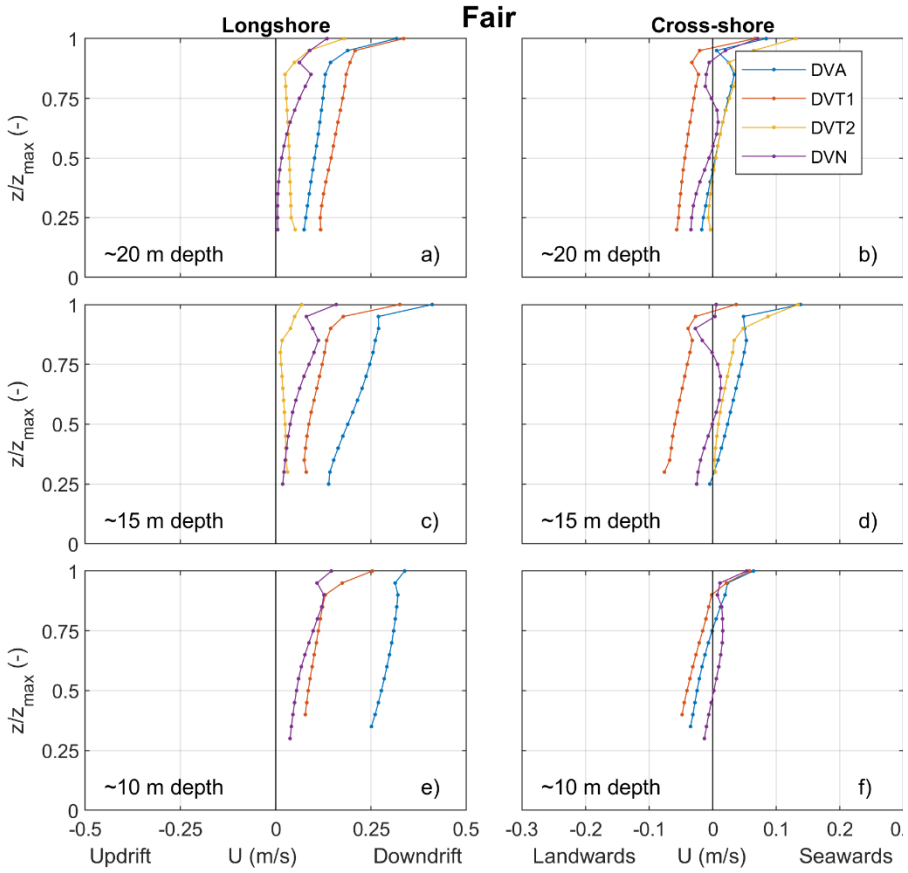

Figure 3.16 Time-averaged residual current profiles during fair-weather conditions, for different depths (columns) and different measurement campaigns (colours). Profiles are shown for non-dimensional depth (z/z_{max}) to allow for comparison of different water depths.

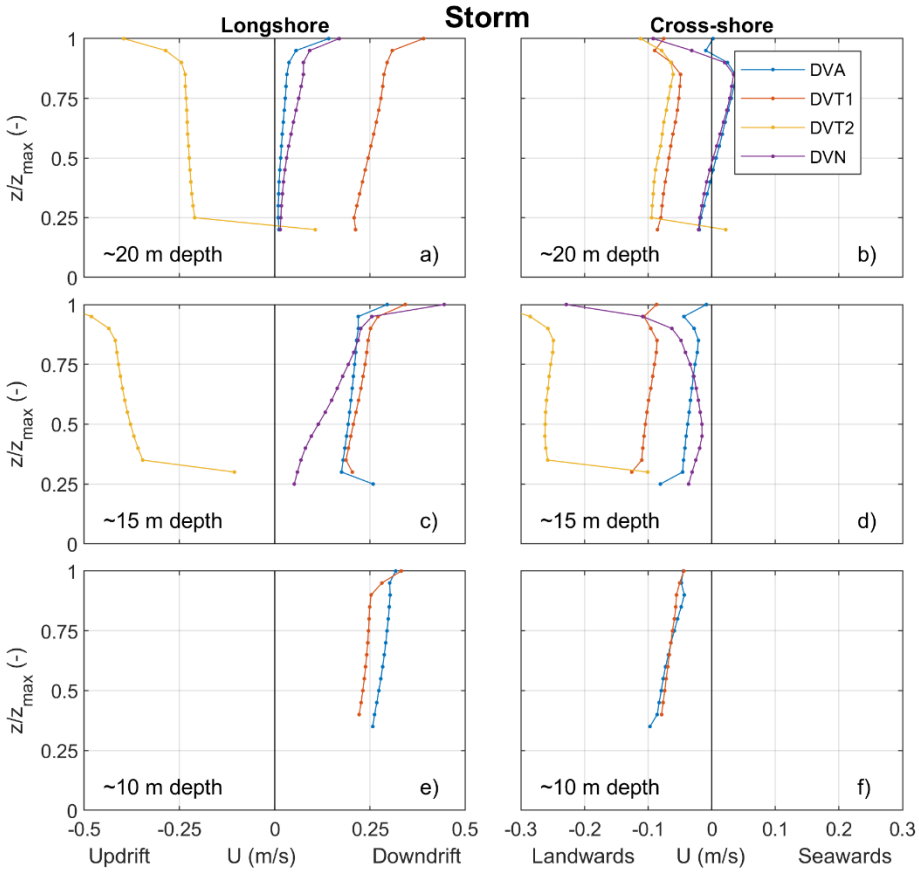

Figure 3.17 Time-averaged residual current profiles during storm conditions, for different depths (columns) and different measurement campaigns (colours). Profiles are shown for non-dimensional depth (z/z_{max}) to allow for comparison of different water depths.

4 Bedforms

4.1 Observed bedforms

4.1.1 Observed transport regimes

Wave orbital velocities derived from integral wave parameters (Section 3.1) and observed mean currents were used to derive wave- and current-related Shields parameters to assess the relationship between observed bed forms and hydrodynamic forcing conditions. Figure 4.1 shows the range in wave- and current-related Shields parameters that was found in the present study. This figure shows that the dataset consists of observations of bedforms under a wide range of conditions, which makes it truly unique. Wave-dominated, current-dominated, no motion and sheet flow conditions occurred. A large part of the data are wave-current dominated, which is mainly true for the AZG and DVA campaigns. The DVT1 and DVT2 campaigns were more current-dominated, and at the DVN campaign the threshold of motion was rarely exceeded. This is mainly caused by the fact that most of the DVT and DVN data were acquired at 20 m water depth, so waves could not reach the bed.

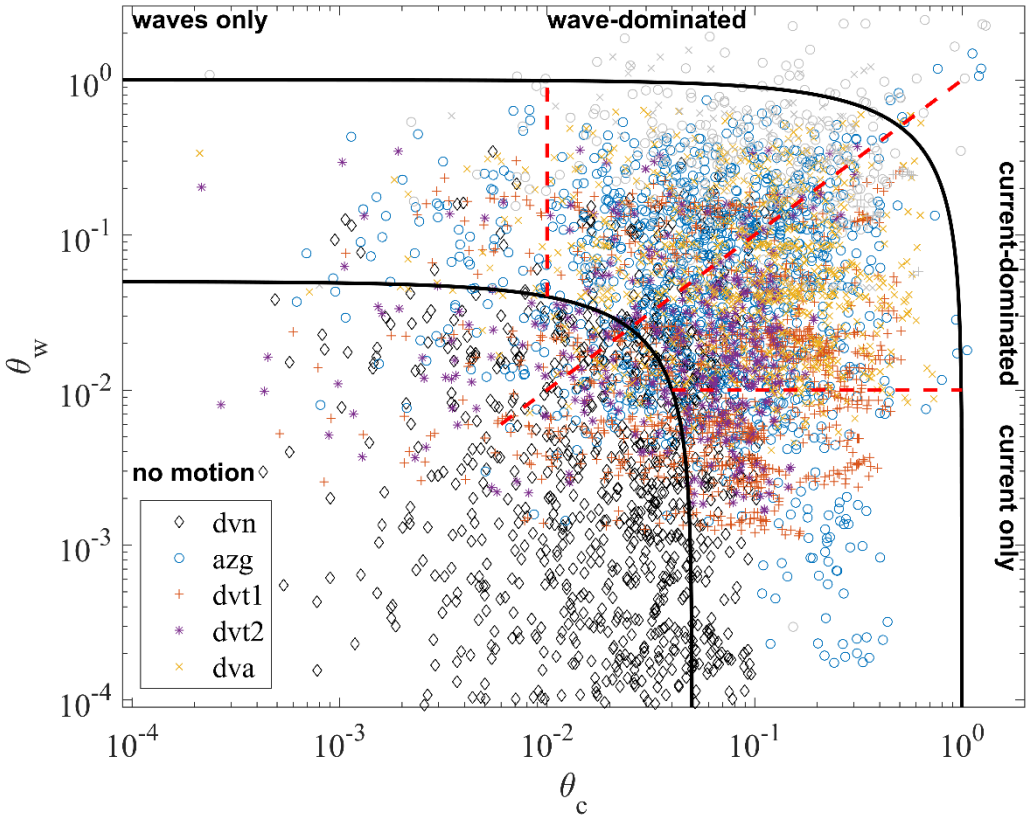

Figure 4.1. Measured wave- versus current-related Shields stress for all campaigns. Black lines indicate sheetflow and incipient motion. Red dashed lines show the boundaries between regions of wave or current dominance, according to Kleinhans (2005). Grey data points indicate moment with no SONAR data.

4.1.2 Typical bedforms observed at the lower shoreface

Figure 4.2 shows 2D histograms of ripple heights and lengths for all frames separately, and for all data together. The black line denotes the equilibrium steepness η/λ =0.16 (e.g. Wiberg and Harris, 1994; Camenen, 2009). The average height and length are given by the red cross.

Ripple heights of 0.01 to 0.03 m were found, and ripple lengths range between 0.08 and 0.20 m. On average, the ripples are 1.55 cm high and 12 cm long. This implies that most of the time, their steepness is smaller than the equilibrium steepness of 0.16. Wave lengths are smallest at the DVA and AZG campaigns, which also results in the highest steepness values here. The ripples are the least steep at DVN, which also had the lowest Shields parameters (Figure 4.1). Therefore, this characteristics of the bedforms seems to be more related to the hydrodynamic conditions than due to location. The three-dimensionality of the bedforms (Tb) is always high, values range between 0.94 and 1, with an average of 0.99.

Although the range in η, λ and Tb is small, little variations might be found depending on either (1) water depth, (2) grain size or (3) hydrodynamics. Table 2.3 shows that the larger grain sizes were found at measurement locations with larger water depth. Water depth is related to the hydrodynamics as well, but in line with Chapter 3 we will discuss it separately.

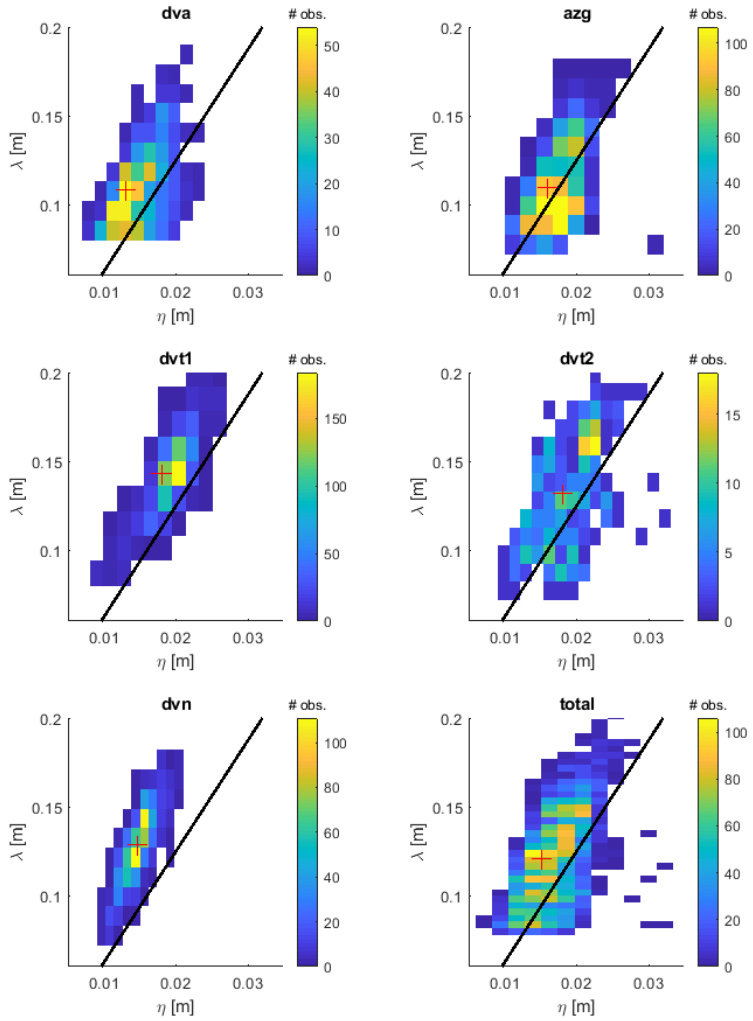

Figure 4.2. 2D histogram of ripple heights and lengths for all frames separately, and for all data together. The black line is the equilibrium steepness η/λ =0.16. The average height and length are given by the red cross.

4.1.3 Variation with depth on the shoreface

While Figure 4.2 already shows some small variations in ripple height along the coast, the differences are better visible when dividing the observations into depth categories. The three depth categories are:
~20 m depth: dva1, dvt11, dvt21, dvn1
~15 m depth: dva3, azg3
~10 m depth: dva4, azg4, dvt24
<10 m depth: azg1, azg5 (these frames are technically not on the lower shoreface, therefore they will be marked grey from Figure 4.4 onwards).

Figure 4.3 shows that with increasing depth, the ripple height does not change, but the ripple length increases. This might be caused by the larger (range in) grain sizes at this depth, as Soulsby and Whitehouse (2005) found that λ increases with grain size until a D_{50} of 0.4 mm, which is similar to the maximum grain size in the present study. Since η is constant, the ripple steepness and bed roughness decrease with depth.

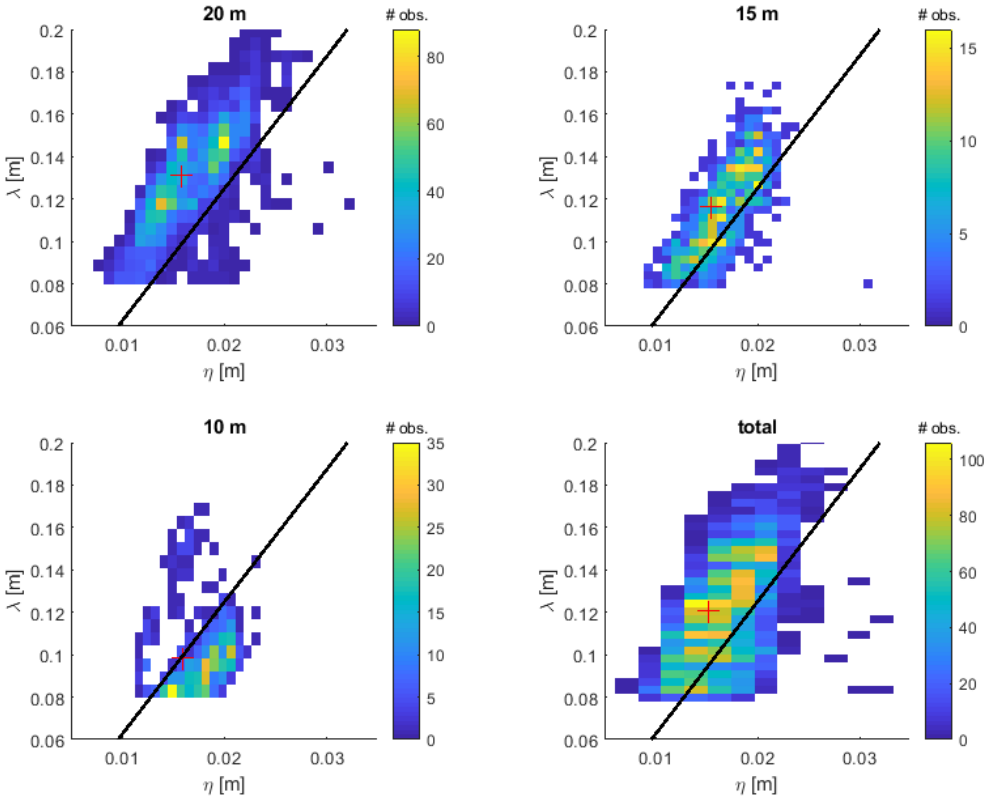

Figure 4.3. 2D histograms grouped by depth at which the frames were placed. The black line is the equilibrium steepness η/λ =0.16. The average height and length are given by the red cross.

Figure 4.4 shows that, even though Tb is always high, visually some two-dimensionality occurs sometimes. Yet, because the variance is high both parallel and perpendicular to the ripple crests, the minimum Tb is still 0.95. Around 10 m depth, there is an absence of this two-dimensionality, whereas Tb shows quite a large spread at both deeper and shallower water. The increasing spread with depth at h>10 m might be related to the fact that the lower shoreface is more current-dominated, while the upper shoreface is wave-current dominated.

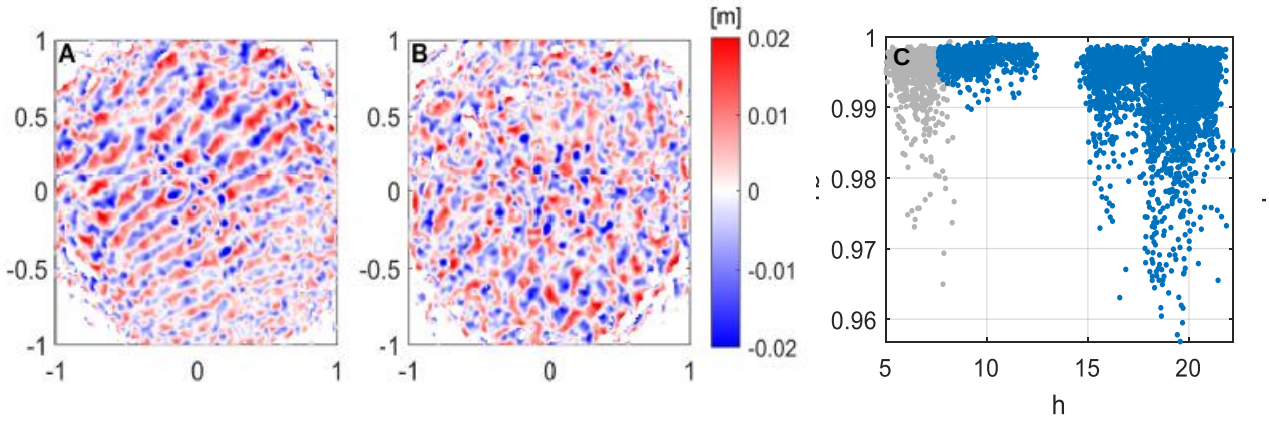

Figure 4.4. Examples of ripples with Tb = 0.95 (A) and Tb = 1 (B). C: Ripple three-dimensionality against water depth

4.1.4 Effect of hydrodynamics and Shields parameter

Figure 4.5 shows the hydrodynamics and ripple height and wavelength through time measured at Frame 1 of the DVT1 campaign. Wave heights were low at first, but between 16 and 18 January, they increased, and became over 2 m high. Simultaneously, the wave orbital velocity and wave mobility also increased. It is visible that in the same time period, the ripple height and wavelength decreased. Aside from that period, the ripple height is relatively constant: variations on the time scale of the tides are not found. The ripple wavelength is more variable: a relation between the ripple wavelength and the depth-averaged current velocity is especially visible between 16 and 20 January. The hydrodynamics and ripple characteristics through time of all other frames and campaigns can be found in Appendix B.

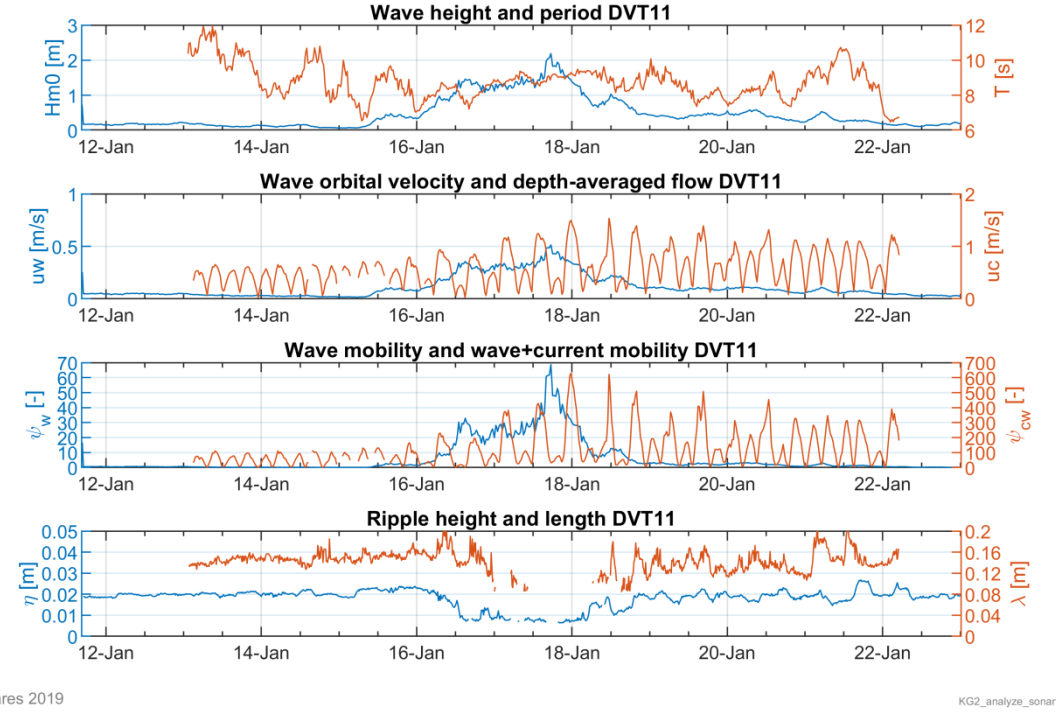

Figure 4.5. Hydrodynamics (upper three plots) and ripple height and wavelength (lowest plot) through time for Frame 1 of the DVT1 campaign.

We now test the effects of wave conditions on the ripple characteristics by comparing ripple height η and ripple length λ to the wave-orbital velocity u_w and the wave orbital excursion A_w (without making the hydrodynamic conditions dimensionless). Figure 4.6 shows the ripple height η versus the orbital velocity (left) and ripple height versus orbital excursion (right) for different depths. As shown in Chapter 3, the wave orbital velocities (u_w) range between a few mm/s and more than 1 m/s. The wave orbital excursions A_w range between a few mm and more than 1.5 m. No differences in η were found between the different depths. Ripple height generally decreases with wave orbital motion, which corresponds to the behaviour of bedform predictors such as the one by Nielsen (1981) or Grasmeijer & Kleinhans (2005) for wave mobility numbers $\psi_w > 10$. Comparison with predictors will be made in Section 4.3.

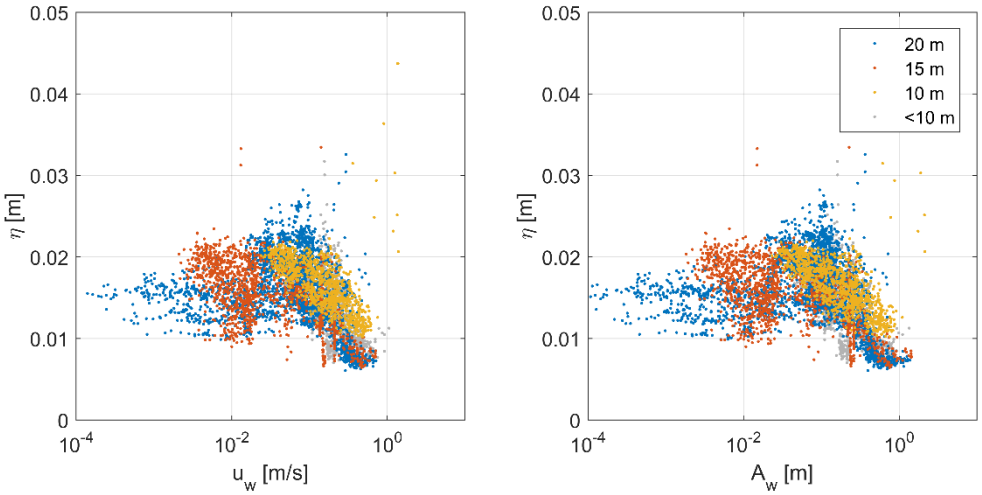

Figure 4.6. Ripple height versus orbital velocity (left) and ripple height versus orbital excursion (right).

Figure 4.7 shows the ripple length λ versus both wave orbital parameters. As also found in Figure 4.2 and Figure 4.3, the observed ripple length λ ranges between about 0.08 m and 0.20 m. A clear relation with the wave orbital motion cannot be observed from this figure.

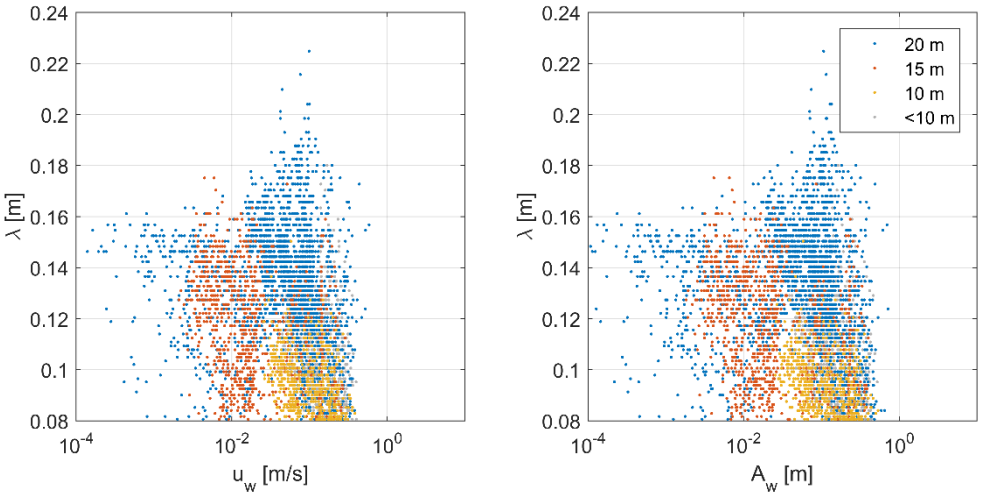

Figure 4.7. Ripple length versus orbital velocity (left) and ripple length versus orbital excursion (right).

We subsequently test the effects of hydrodynamics on the ripple characteristics by comparing η, λ, Tb and k_s (here taken as $k_s = \eta^2/\lambda$) to the dimensionless wave- and current-related Shields parameters θ_w and θ_c, or the wave-related mobility parameter ψ_w. These parameters include the effects of grain size D_{50}. Figure 4.8 shows that η decreases and Tb increases with increasing θ_w, so ripples become lower and more three-dimensional with increasing wave-related mobility. Interestingly, the decrease rate seems to depend on depth as well: ripple height η decreases faster at 20 m depth than at 10 m depth. Ripple length λ shows no clear effect of mobility although a slight decrease might be perceived. The decrease in both η and λ results in a decrease in bed roughness k_s on the upper part of the lower shoreface.

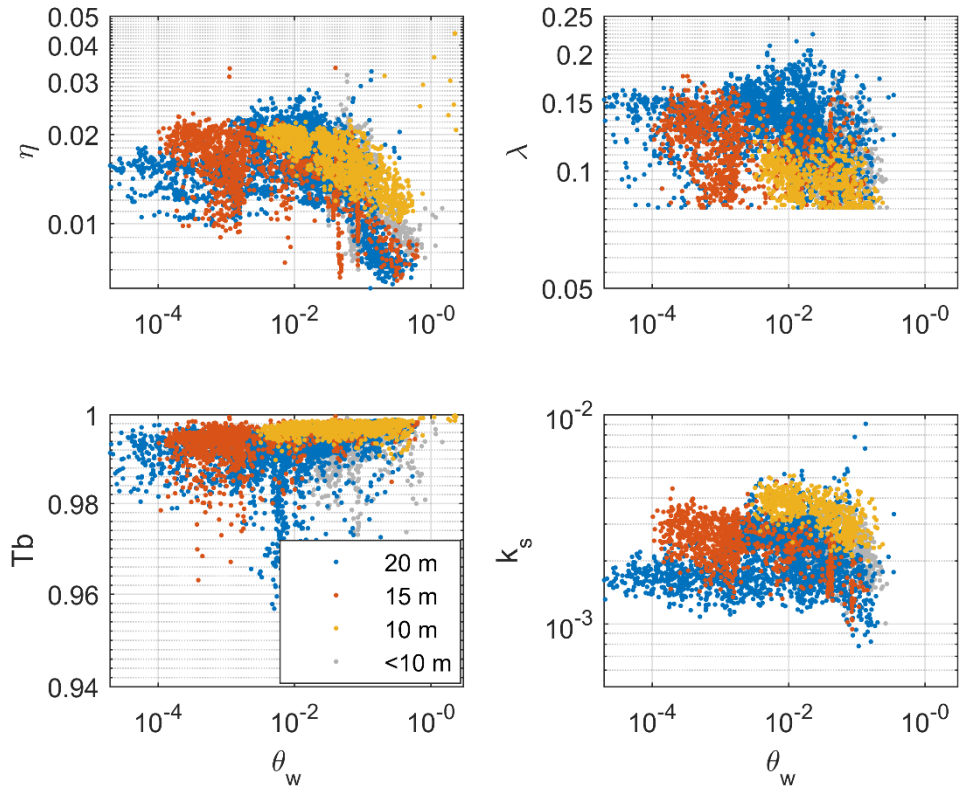

Figure 4.8. Ripple characteristics versus wave-related Shields parameter θ_w

Figure 4.9 shows that the ripple height and length show no clear dependency on the current-related Shields parameter θ_c. The three-dimensionality Tb shows more scatter with increasing θ_c, so the ripples can become more two-dimensional when currents are stronger, but this effect is only visible at depths of 20 m.

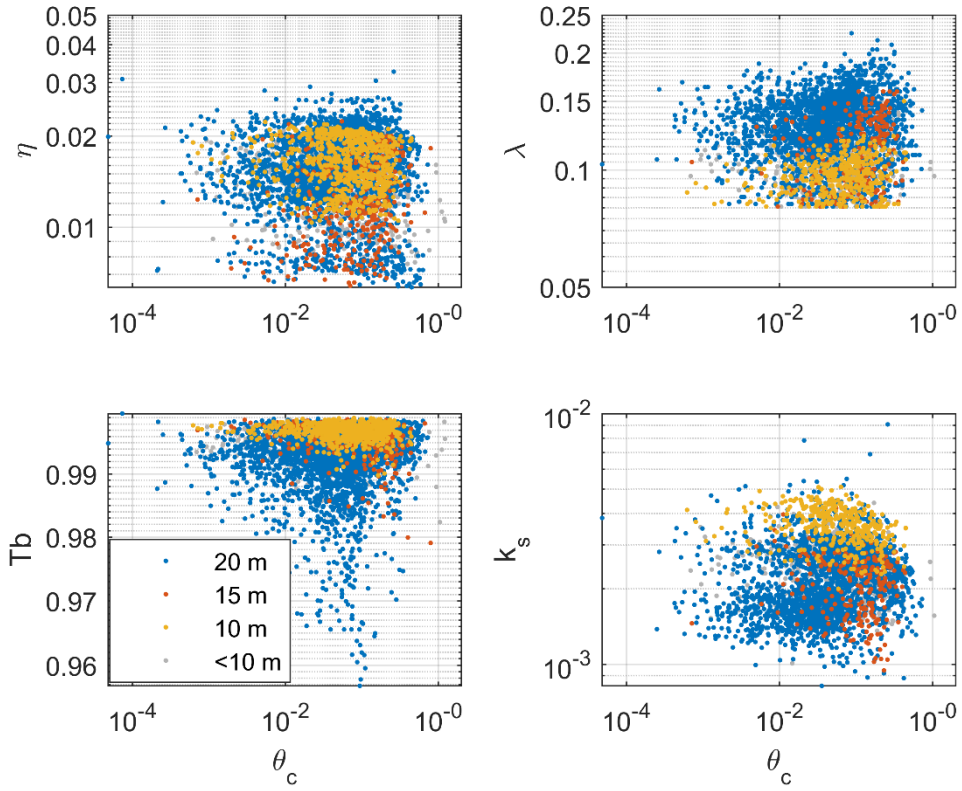

Figure 4.9. Ripple characteristics versus current related Shields parameter θc.

4.2 Comparison with bedform predictors

Figure 4.10 shows the predictive capability of the Van Rijn (2007) and Soulsby et al. (2012) predictors. Van Rijn uses only three input variables: u_w, u_c and D_{50} whereas Soulsby et al. use H_{m0}, h, T, and a time step in addition to that. Even though Soulsby et al. use more input variables, this does not seem to improve the results. With both predictors, the range in predicted ripple heights is much larger than the range in observed heights. A large part of the ripple heights is overestimated by both predictors. The accuracy of both predictors is similar: for Van Rijn, 53% of predicted values is within a factor of 2 of the measured values, and for Soulsby et al. this percentage is 57%. (In comparison, if a constant value of 1.5 cm would be predicted, it would be within a factor of 2 for 97% of the time). Yet, while all predicted heights occur roughly equally using Van Rijn (2007), they are more clustered using Soulsby et al. (2012). The main difference between the various depths is the fact that the predicted ripple heights at 20 m depth can become almost twice as high as those predicted at other depths. This is likely caused by the larger grain sizes at these depths, as they are used as input in both predictors.

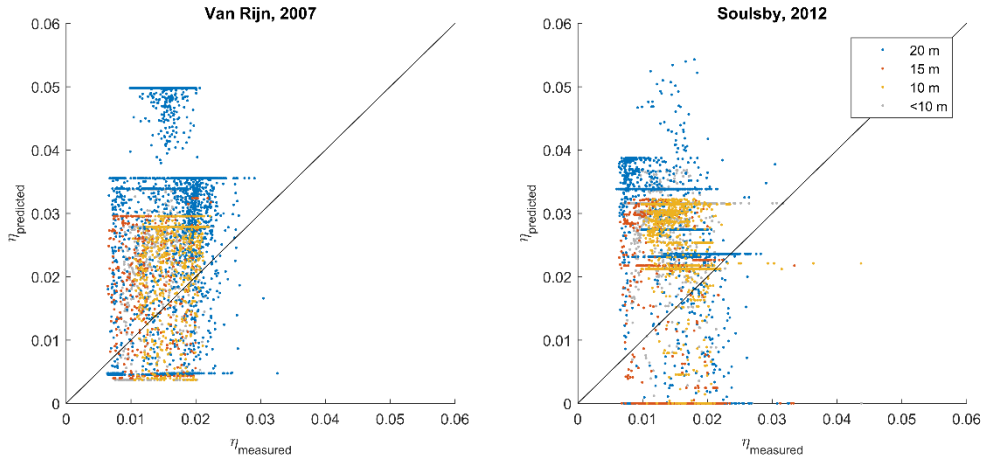

Figure 4.10. Predictive capability of Van Rijn (2007) and Soulsby (2012).

To find out whether the overprediction of the ripple heights is random or systematic, the measured and predicted ripple heights were studied through time for the DVA site. Figure 4.11 shows that the predictions of Van Rijn (2007) are highly dependent on tidal conditions, which are represented in this formula by the depth-averaged current velocity u_c. Besides that, the trends are more or less correct: although they are almost constantly overpredicted, on average (when tidal variations are omitted from the predictions) measured and predicted ripple heights increase simultaneously at all depths. Because of the implementation of the time evolution, the predictor of Soulsby et al. (2012) is more stable than Van Rijn. Most of the predicted changes in ripple height are gradual and take more than one tidal cycle. Yet, this predictor also creates a far too large range in ripple heights.

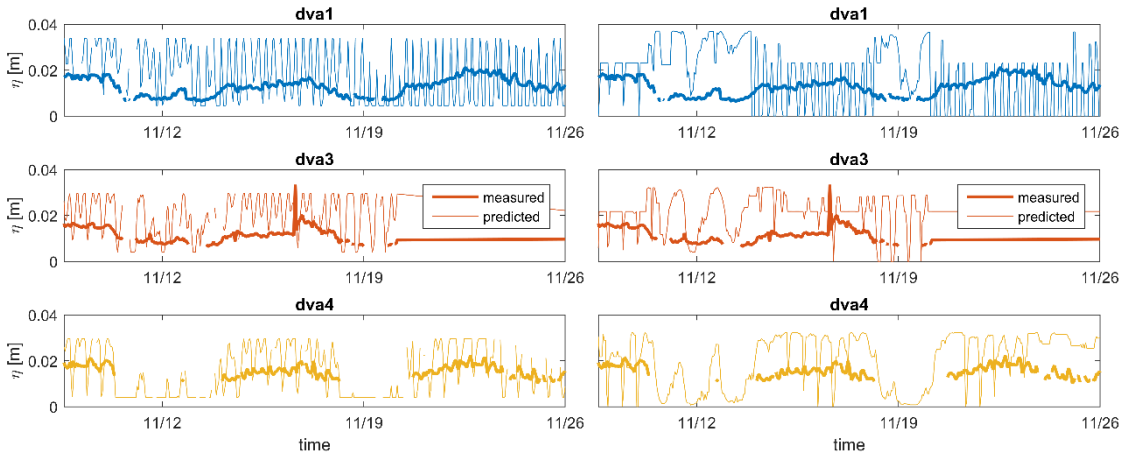

Figure 4.11. Measured (thick lines) and predicted (thin lines) ripple heights through time for Van Rijn (2007) (left column) and Soulsby et al. (2012) (right column).

Figure 4.12 shows the nondimensional ripple height η/A_w as a function of the wave mobility number ψ_w. The data are similar to those in Figure 4.8, in the sense that the relative ripple height decreases with increasing wave importance. This was found in literature as well. For example, Soulsby and Whitehouse (2005) found that the relative ripple height (in their case described by η/H_{m0}) decreased for increasing mobility numbers ψ, which would in this case be synonymous to decreasing water depth (Nielsen, 1979).

The thin lines in Figure 4.12 denote ripple height predictions using the Grasmeijer & Kleinhans (2004) and Van Rijn (1993) models. It is clear that the large extent of the acquired dataset can help to improve ripple height predictor models such as these. In Grasmeijer & Kleinhans (2004), the minimum value that was found of ψ_w, was approximately 1, whereas ψ_w in this dataset starts at values of 10^{-12}.

We derive a new predictor using the data collected in this project. A best-fit line through the measured data points can be described by the following equation:

$$\frac{\eta}{A_w} = 10^{-0.5762 \log \psi_w - 0.6818}$$

This new predictor has an r^2 of 0.96, so the predicted heights are close to the measured ones. On top of that, the right part of Figure 4.12 shows that ripple heights are much more stable, because the depth-averaged current velocity (the effect of the tide) is not incorporated in the formula. However, the trends are not predicted correctly: for example, around 19 November, the measured ripple height at DVA1 decreases, while the predicted one increases. This means that some physical terms are still missing in the new predictor. The percentage of values within a factor 2 of the measurements is 96%, which is much higher than the values that were found for Soulsby et al. (2012) and Van Rijn (2007), but the use of a constant value for ripple height is equally predictive.

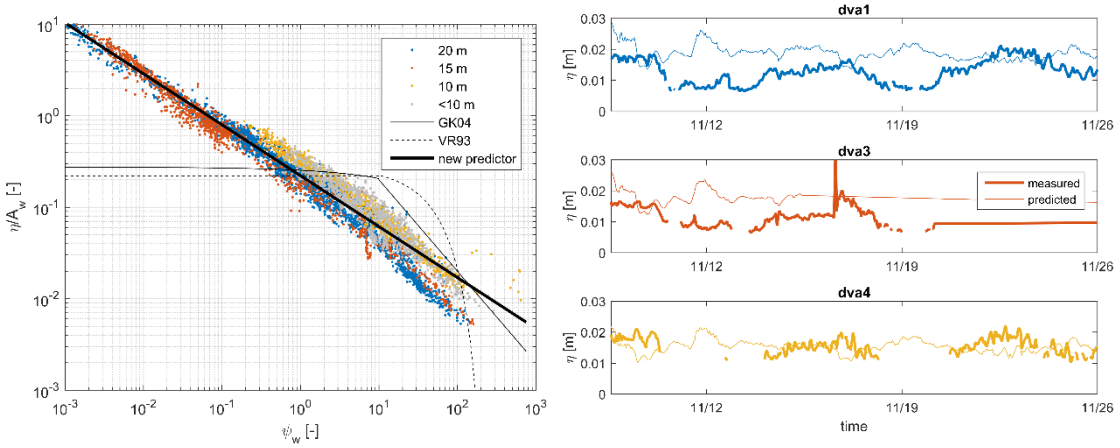

Figure 4.12. Left: Nondimensional ripple height versus wave mobility number. Lines denote the Grasmeijer & Kleinhans (2004) and Van Rijn (1993) model curves. The thick black line is the proposed new model. Right: measured and predicted ripple heights by the proposed model through time.

Figure 4.13 shows the ripple steepness η/λ as a function of the wave mobility number ψ_w. At all depths, the steepness is more or less constant, with a total average of 0.14. Not only for ψ_w<10, as the predictors of Grasmeijer and Kleinhans (2004) and Van Rijn (1993) suggest, but also for ψ_w>10. Because of the small λ, the steepness at 10 m water depth is largest, as explained before. This variability is not incorporated in either of the predictors. Yet, the only improvement that can be made is assuming a constant steepness value of approximately 0.14 for all values of ψ_w.

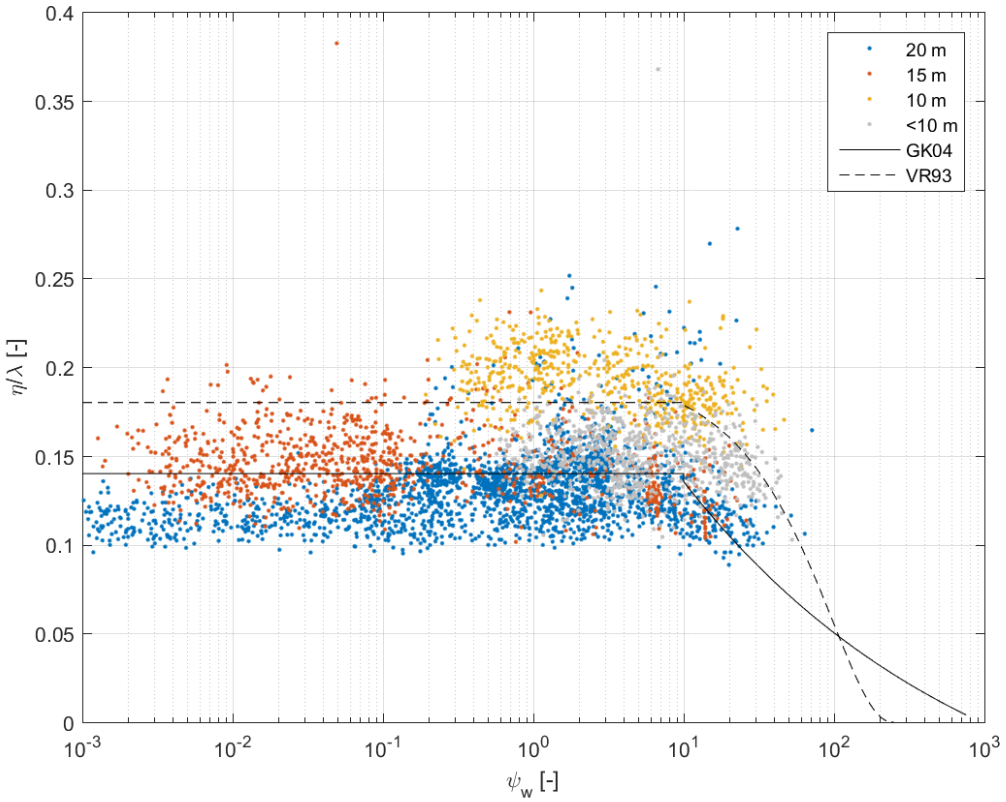

Figure 4.13. Ripple steepness versus wave mobility number. Lines denote the Grasmeijer & Kleinhans (2004) and Van Rijn (1993) model curves.

5 Discussion

We found that the near-bed orbital velocities scale linearly with the local significant wave height and, as a result, should be estimated well using linear wave theory. In this study there is, however, an underestimation of the near-bed orbital velocities derived from surface wave parameters, especially at the lower part of the lower shoreface. This is, however, attributed to an underestimation of the significant wave height in the processing of the pressure transducer observations (because the dynamic pressure is not captured well in these data). The underestimated near-bed orbital velocity amplitudes are used in the bedform analysis which influences the results, specifically the results that show the change in bedform dimensions versus wave intensity (Figure 4.1 and Figure 4.5 - Figure 4.9). The analysis can be improved by using other data sources for an estimation of the near-bed orbital velocity. This can be derived from the ADV observations (but results in data loss) or from surface wave characteristics derived from the wave transformation matrix (but introduces modelling errors). Moreover, the near-bed orbital velocities derived from the PT surface wave characteristics show a relative constant bias with the orbital velocities derived from the ADV. Therefore, the results would show a constant increase in wave dominance. Such a change in the results would not lead to different qualitative conclusions. Furthermore, the performance of the bedform predictors is not likely to show major improvement by such a change as well because the major flaw of the predictors is the highly fluctuating motion of the predicted bedform dimensions and not a constant under estimation due to wave dominance.

The skewness and asymmetry derived from the ADV observations compare well to the Ruessink et al. (2012) parametrization. The observed values are, however, likely to be underestimated due to the applied moving average window of 25 samples and further testing with different settings should be done to conclude on the applicability of the parametrization for the lower shoreface.

The residual currents found at the lower shoreface show correlation to the wave and wind conditions. A detailed process-analysis on the causality of the residual currents was not the scope of this study but a first assessment has been made by a linear regression analysis. The results show that during very energetic conditions the wave energy (E_w) and the depth averaged current strength correlate well, which indicates a dependency on the wave conditions. Using (3D) process-based models to compare Stokes drift-driven residual flow allows a detailed analysis on processes. However, the cross-shore velocity profile during storm conditions (Figure 3.17) does not match the theoretical profile (Figure 2.6) and the models are therefore expected to underestimate the landward directed cross-shore current at the lower shoreface. This underestimation was actually also found in modelling efforts that were part of the KG2 programme (Grasmeijer et al., 2019). This study did, however, only consider depth-averaged currents in the comparisons. Further analysis on the modelled depth-varying velocity profile on the lower shoreface can improve insights on the lower shoreface hydrodynamics during storm conditions.

6 Conclusions and recommendations

Conclusions

The objective of this study was to give an analysis on the spatial and temporal variability of wave-induced (near-bed) orbital motion, residual (non-tide driven) currents, and small-scale bedforms at the Dutch lower shoreface. The conclusions are given by providing answers to the research questions.

1. *What are characteristic values for the near-bed wave orbital amplitude and net (residual) velocities on the lower shoreface of Ameland, Terschelling, and Noordwijk*

   Characteristics orbital velocities (orbital velocity amplitudes) on the Dutch lower shoreface are in the order of a few dm/s but can reach up to 1 m/s when the relative wave height (H_s/h) attains a value of ~0.3. The maximum observed orbital velocity is ~0.8 m/s at the lower part (20 m water depth) and >1 m/s at the shallower part (15 m water depth).

   Characteristic residual (depth averaged) velocities on the lower shoreface are in the order of a few dm/s in longshore direction and a few cm/s in cross-shore direction. During energetic wind or wave conditions the residual current can exceed 0.5 m/s in longshore direction and up to ~0.4 m/s in cross-shore direction.

2. *How do the near-bed wave orbital motion and residual velocities vary with depth, wave, and wind conditions?*

   The near-bed wave orbital velocity scales linearly with the significant wave height, which increases with shallower depths (which also follows from linear wave theory). Waves are not asymmetric on the lower shoreface but become skewed during energetic wave conditions ($Ur > 10^{-2}$).

   Residual velocities on the lower shoreface are significantly altered from the tide-driven flow during energetic wind and (non-breaking) wave conditions. During these conditions the strength of the residual current increases with decreasing depth and increases with the intensity of the wind and wave conditions. This can be described well by a linear relation of the depth-averaged residual current strength with wave energy. These relations are, however, not valid for less energetic conditions. The residual current velocity profile during observed energetic conditions is completely landward directed over the complete water column, which is a significant change from the mild conditions where the profile varies from landwards at the surface to seawards lower in the water column (in accordance to a Stokes drift driven profile).

3. *How does the observed near-bed wave orbital motion compare to a well-established parametrization (i.e., Ruessink et al., 2012)?*

   The parametrization presented by Ruessink et al., 2012 describes wave skewness and asymmetry on the lower shoreface well, even for wave conditions that are far less non-linear than the conditions used to establish the relation.

4. *What are the characteristic bedforms found on the lower shoreface?*

   On the lower shoreface, the full range of transport conditions (no motion, wave-current dominated, and sheet flow) were observed. The dimensions of the accompanying bedforms (ripples) range between 0.01 – 0.03 m in bedform height (η) and 0.08 – 0.20 m in bedform length (λ). The majority of the bedforms found are less steep than the equilibrium steepness (η/λ =0.16). The 3-dimensionality of the bedforms can be expressed by a dimensionless parameter (T_b) that ranges between 0 – 1. This parameter is always high (0.94 – 1) for the observed bedforms and has an average value of 0.99 (i.e., highly 3-dimensional).

5. *How do the bedforms vary with location, depth and wave conditions?*

   Moving up the lower shoreface (decreasing water depth) the wave length of the bedforms decreases. The bedform height, however, is more-or-less equal over the depth range studied, which results in steeper ripples with decreasing depth. The 3-dimensionalty of the bedforms increases as well with decreasing water depth.

   The bedform height decreases with an increase in the wave orbital motion. In general, an increase in the wave mobility (dependent on grain size as well) results in lower and more 3-dimensional bedforms. The rate of change, however, depends on water depth; the rate is faster in deeper water. An increase in the strength of the current results in more 2-dimensional bedforms.

   Besides the hydrodynamic forcing conditions and water depth, the bedform dimensions vary between locations. Bedforms have the smallest wavelengths at Ameland (resulting in the steepest bedforms) and are the flattest (less steep) at Noordwijk. The bedforms found at Noordwijk are flat because the threshold of motion is rarely exceeded (flat-bed). Therefore, this seems more related to hydrodynamic conditions then geographic location.

6. *How do the bedform characteristics derived from field observations compare to the characteristics derived via established formulations (e.g. Van Rijn, 2007)*

   The Van Rijn (2007) and Soulsby et al. (2012) bedform predictors are tested. Both predictors do not perform well: the predicted range in bedform height is much larger and in general overestimated. The Soulsby et al. (2012) predictor does produce more stable results (less dependent on fluctuating tidal conditions) because relaxation effects are included by using the time step as input parameter.

7. *What concepts can be derived from the analysis and do they confirm our conceptual understanding of lower shoreface morphodynamics?*

   The analysis adds the following to our conceptual understanding of lower shoreface hydro- and morphodynamics:
   - During energetic wind and wave conditions the observed cross-shore velocity profile changes from a depth-varying profile to a profile that is completely in landward direction over the water column;
   - Bedforms are highly 3-dimensional and dimensions are quite constant in time. This is one of the reasons bedform predictors fail because they are highly dependent on the fluctuating current conditions.

6.1 Recommendations

The scope of this study was to analyse the temporal and spatial variability of hydrodynamics and bedforms on the lower shoreface. Therefore, an in-depth analysis on causality and explanatory variables was not part of the analysis. Future research should focus on this by:

- Studying the relation between residual currents at the lower shoreface and the driving (wave-induced) processes. For this purpose, a first assessment can be made on the correlation between direction of the residual currents and the local wave conditions as an indicator of wave importance;
- Quantifying residual currents based on the wind and wave conditions in more detail;
- Performing 3D modelling to test the hypotheses that can be drawn from the analyses from the two points above in relation to residual currents. Furthermore, this allows for an in-depth analysis of the change in velocity profile between mild and energetic conditions.

Above described analysis will increase our understanding on the role of residual currents on lower shoreface dynamics which will, in turn, enhance our predictive capabilities of lower shoreface processes as residual currents are underestimated in existing models.

Besides the points above for future study, an additional analysis on the comparison of observed and parametrized skewness and asymmetry should be done using other settings to derive the observed parameters (the present settings give an underestimation).

At last, the analysis of the data acquired results in a few recommendations on performing field measurements on the lower shoreface:

- Future SONAR observations should be performed on a smaller temporal resolution (e.g. 15 min) to allow the analysis of bedform migration which can be a proxy for bed load transport.
- The present analysis of bedforms shows an interlinked dependency on water depth and grain size. Future field campaigns should try to isolate (decouple) the effect by selection of field sites to allow for an explanatory analysis.
- To improve our understanding of (wave-induced) sediment transport patterns on the lower shoreface observations of the wave boundary layer and sediment transport are required at very close proximity of the bed.

7 References

Abreu, T., Silva, P., Sancho, F., & Temperville, A. (2010). Analytical approximate wave form for asymmetric waves. In Coastal Engineering (Vol. 57). https://doi.org/10.1016/j.coastaleng.2010.02.005

Brakenhoff, L.B., Kleinhans, M.G., Ruessink, B. G., & Van der Vegt, M. (2019). Spatio-temporal characteristics of small-scale wave-current ripples on the Ameland ebb-tidal delta. Submitted.

Brakenhoff, L., Van der Vegt, M., & Ruessink, G. (2019). Local spatio-temporal bedform patterns on an ebb-tidal delta. Marine and River Dune Dynamics – MARID VI, (1-3 April), 17–22. Bremen, Germany.

De Boer, G. J. (2009). On the interaction between tides and stratification in the Rhine Region of Freshwater Influence. Retrieved from http://www.narcis.nl/publication/RecordID/oai:tudelft.nl:uuid:c5c07865-be69-4db2-91e6-f675411a4136%5Cnhttp://repository.tudelft.nl/view/ir/uuid:c5c07865-be69-4db2-91e6-f675411a4136/

Boxel, J. H. van, Sterk, G., & Arens, S. M. (2004). Sonic anemometers in aeolian sediment transport research. Geomorphology, 59(1–4), 131–147. https://doi.org/10.1016/j.geomorph.2003.09.011.

Camenen, B. 2009. Estimation of the wave-related ripple characteristics and induced bed shear stress. Estuarine, Coastal and Shelf Science 84 (4): 553–564. doi:10.1016/j.ecss.2009.07.022.

Grasmeijer, B. (2018). Method for Calculating Sediment Transport on the Dutch Lower Shoreface. Delft, The Netherlands.

Grasmeijer, B. T., & Kleinhans, M. G., 2004. Observed and predicted bed forms and their effect on suspended sand concentrations. Coastal Engineering, 51(5–6). doi: 10.1016/j.coastaleng.2004.05.001

Grasmeijer, B., Schrijvershof, R., & Van der Werf, J. (2019). Modelling Dutch Lower Shoreface Sand Transport. Delft, The Netherlands.

Grinsted, A., J. C. Moore, and S. Jevrejeva. 2004. Application of the cross wavelet transform and wavelet coherence to geophysical time series. Nonlinear processes in geophysics 11 (5/6): 561–566.

Guo, J. (2002). Simple and explicit solution of wave dispersion equation. Coastal Engineering, 45(2), 71–74. https://doi.org/10.1016/S0378-3839(02)00039-X

Leummens, M. (2018). Hydrodynamics and sand transport on the lower shoreface of the Ameland tidal inlet. Retrieved from https://www.utwente.nl/en/et/wem/education/msc-thesis/2018/leummens.pdf.

Niedoroda A.W., Swift D.J.P, Hopkins T.S. (1985) The Shoreface. Coastal Sedimentary Environments. Davis R.A. {ed.}. New York, NY. Springer – Verlag, (Second Revised, Expanded Edition) 8, pp. 533-624

Nielsen, P. 1979. Some basic concepts of wave sediment transport. Series Paper 20.

Nielsen, P. 1992. Coastal bottom boundary layers and sediment transport. Singapore: World Scientific Publishing Co. Pte. Ltd.

Núñez-González, F., D. Hesse, B. Ettmer, and O. Link. 2014. Objective method for ranking bedforms with a 3-dimensionality-index. In River flow, ed. Schleiss et al., 1059–1065. Taylor & Francis Group, London.

Pawlowicz, R., Beardsley, B., & Lentz, S. (2002). Classical tidal harmonic analysis including werror estimates in MATLAB using T_TIDE. Computers and Geosciences, 28(8), 929–937. https://doi.org/10.1016/S0098-3004(02)00013-4.

Ribberink, J. S., & Al-Salem, A. A. (1994). Sediment transport in oscillatory boundary layers in cases of rippled beds and sheet flow. Journal of Geophysical Research: Oceans, 99(C6), 12707–12727. https://doi.org/10.1029/94JC00380

Ruessink, B. G., Ramaekers, G., & Van Rijn, L. C. (2012). On the parameterization of the free-stream non-linear wave orbital motion in nearshore morphodynamic models. Coastal Engineering, 65, 56–63. https://doi.org/10.1016/j.coastaleng.2012.03.006.

Soulsby, R. L. 1997. Dynamics of marine sands. London: Thomas Telford Publications.

Soulsby, R. L., R. J. S. Whitehouse. 2005. Prediction of ripple properties in shelf seas. Mark 1 predictor. Report TR150. HR Wallingford.

Soulsby, R. L., R. J. S. Whitehouse, and K. V. Marten. 2012. Prediction of time-evolving sand ripples in shelf seas. Continental Shelf Research 38: 47–62. doi:10.1016/j.csr.2012.02.016.

Treurniet, B. (2018). Wave orbital motion on the Dutch lower shoreface: observations , parameterizations and effects on bed- load sediment transport.

Torrence, C., and G. P. Compo. 1998. A practical guide to wavelet analysis. Bulletin of the American Meteorological society 79 (1): 61–78.

Van der Werf, J. van der, Grasmeijer, B., Hendriks, E., van der Spek, A., & Vermaas, T. (2017). Literature study Dutch lower shoreface.

Van der Werf, J.J. van der, Álvarez Antolínez, J.A., Brakenhoff, L., Gawehn, M., Den Heijer, K., Meijer – Holzhauer, H., Pearson, S., Van Prooijen, B., Tissier, M., Tonnon, P.K., De Vet, L., Vermaas, T., 2019. Data report Kustgenese 2.0 measurements. Report 1220339-015-ZKS-0004. Rijkswaterstaat, Deltares, Utrecht University, Delft University of Technology, University of Twente.

Van Oeveren - Theeuwes, M. C., Nolte, A., Tonnon, P. K., van der Werf, J. J., & Baart, F. (2017). Plan van Aanpak Kustgenese 2.0 versie januari 2017.

Van Rijn, L. C., 1993. Principles of sediment transport in rivers, estuaries and coastal seas. The Netherlands: Aqua Publications.

Van Rijn, L. C., 2011. Principles of fluid flow and surface waves in rivers, estuaries seas and oceans. The Netherlands: Aqua Publications.

Van Rijn, L. C. 2007. Unified view of sediment transport by currents and waves. i: Initiation of motion, bed roughness, and bed-load transport. Journal of Hydraulic Engineering 133 (6): 649–667. doi:10.1061/(ASCE)0733-9429(2007)133:6(649).

Watanabe, A., & Sato, S. (2005). A sheet-flow transport rate formula for asymmetric, forward-leaning waves and currents. Proceedings of the 29th International Conference on Coastal Engineering, 1703–1714. https://doi.org/10.1142/9789812701916_0136

Wiberg, P. L., and C. K. Harris. 1994. Ripple geometry in wave-dominated environments. Journal of Geophysical Research: Oceans 99 (C1): 775–789.

A Bedform predictors

With Soulsby et al. (2012) and Van Rijn (2007), the actual ripple height is calculated, but many formulas also use nondimensional ripple heights (e.g. Nielsen, 1992; Van Rijn, 1993; Grasmeijer & Kleinhans, 2004) which are often made dimensionless with the wave orbital excursion (equation (10)). The bedform predictors used in this study use these non-dimensional bedform parameters. To illustrate the general behaviour of the predictors, we present the empirical formulae proposed by Grasmeijer & Kleinhans (2004), which are also tested in Chapter 4. The nondimensional ripple height in this formula is expressed as:

$$\frac{\eta}{A} = 2\psi_w^{-1} \qquad \psi > 10 \qquad (21)$$

$$\frac{\eta}{A} = 0.275 - 0.022\psi_w^{0.5} \qquad \psi \leq 10 \qquad (22)$$

The ripple steepness is expressed as:

$$\frac{\eta}{\lambda} = -0.078 + 0.355\psi_w^{-0.221} \qquad \psi > 10 \qquad (23)$$

$$\frac{\eta}{\lambda} = 0.14 \qquad \psi \leq 10 \qquad (24)$$

B Timeseries of ripple dimensions and hydrodynamics

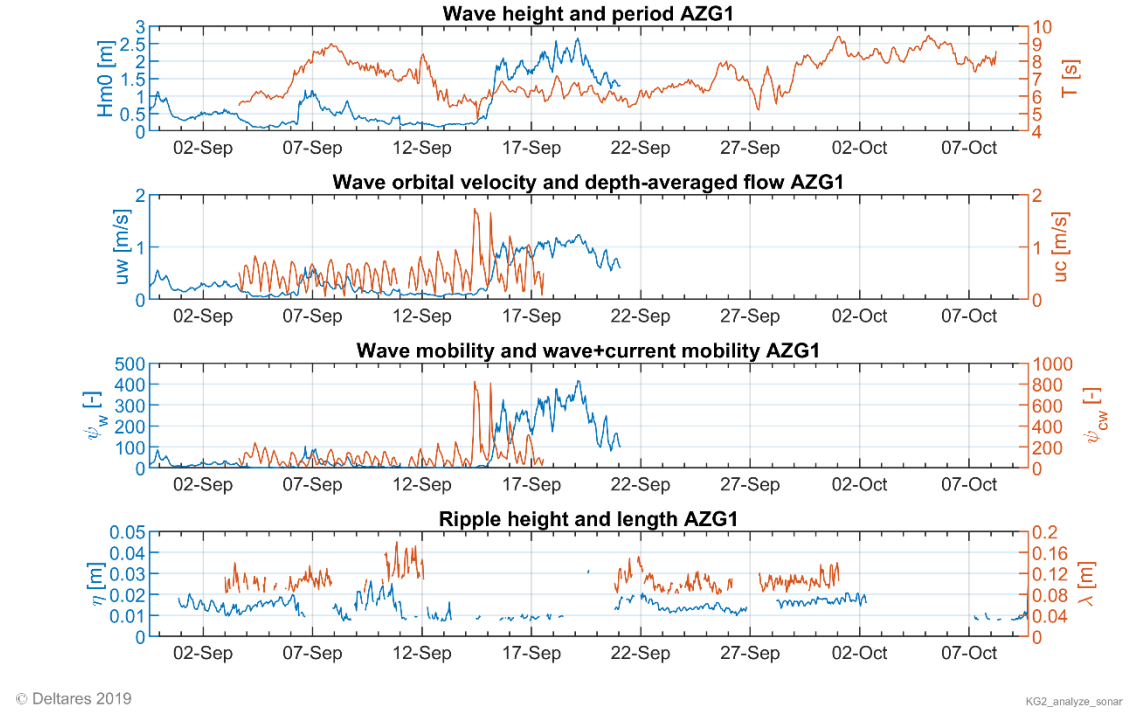

Figure B.1 Timeseries of surface wave characteristics, (wave orbital) velocity, wave and current mobility parameters, and the accompanying bedform dimensions, for AZG-F1.

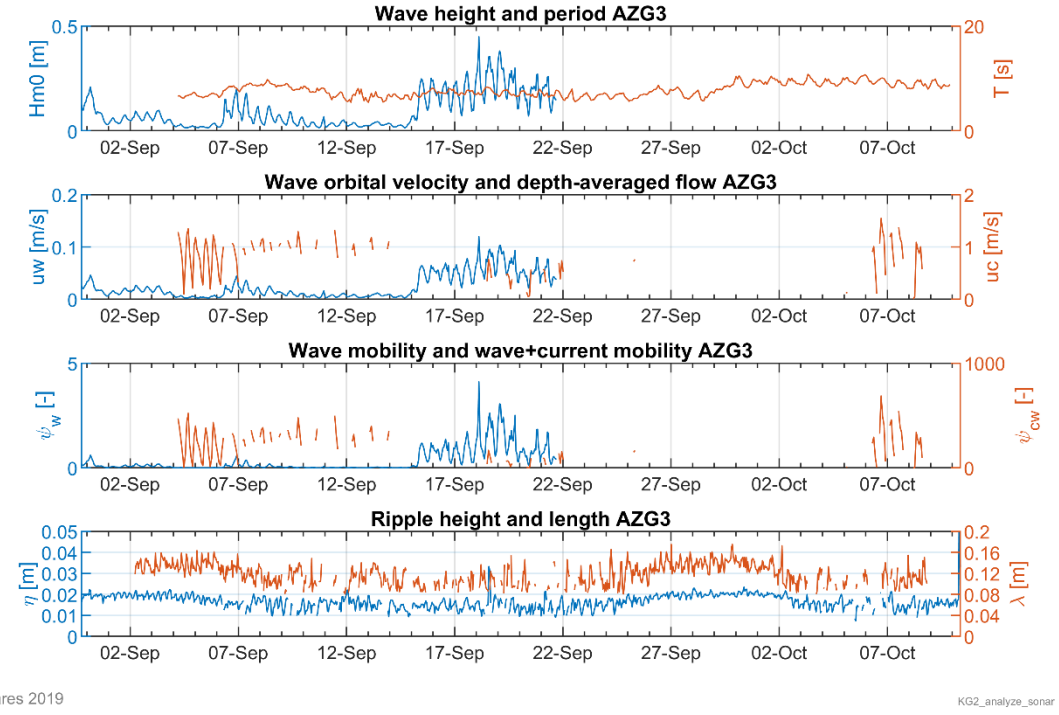

Figure B.2 Timeseries of surface wave characteristics, (wave orbital) velocity, wave and current mobility parameters, and the accompanying bedform dimensions, for AZG-F3.

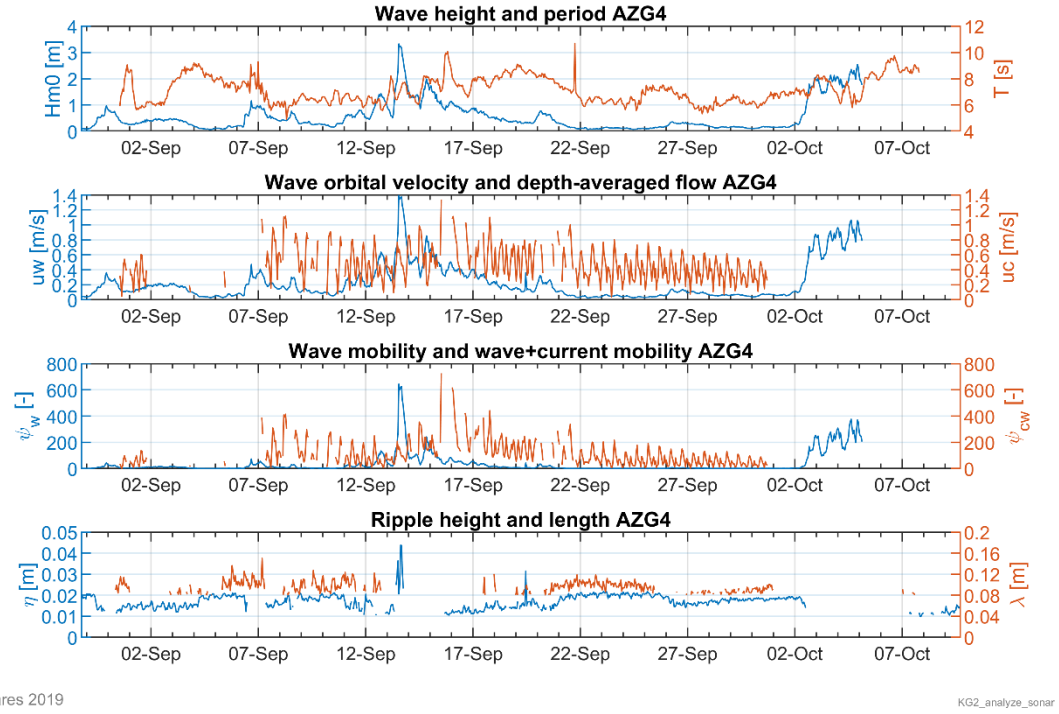

Figure B.3 Timeseries of surface wave characteristics, (wave orbital) velocity, wave and current mobility parameters, and the accompanying bedform dimensions, for AZG-F4.

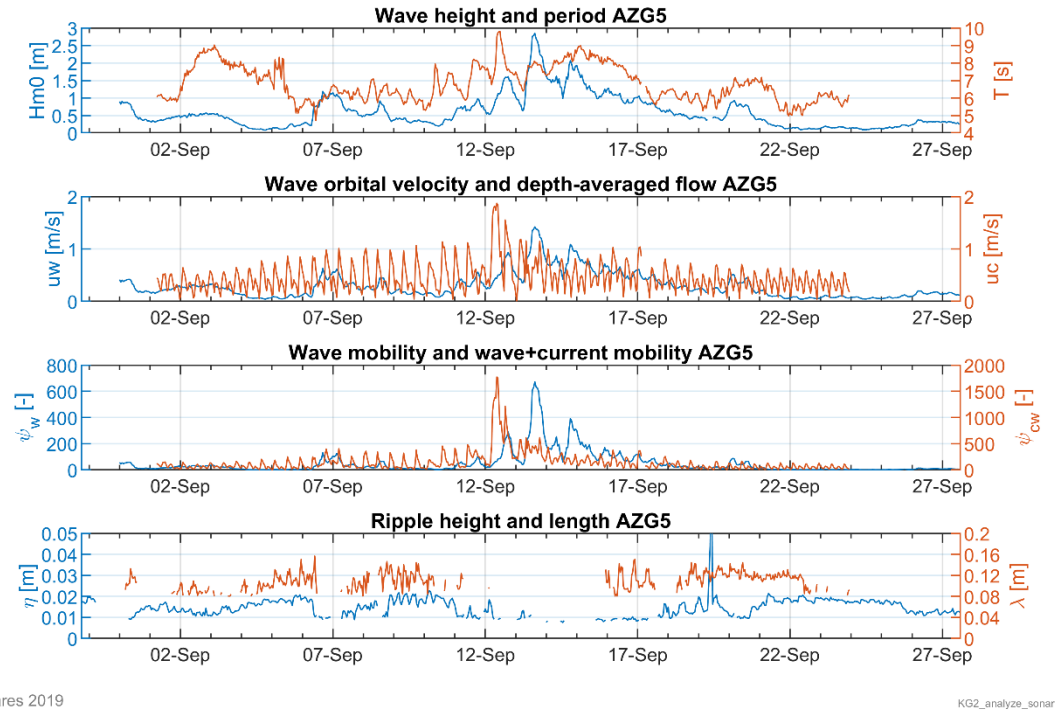

Figure B.4 Timeseries of surface wave characteristics, (wave orbital) velocity, wave and current mobility parameters, and the accompanying bedform dimensions, for AZG-F5.

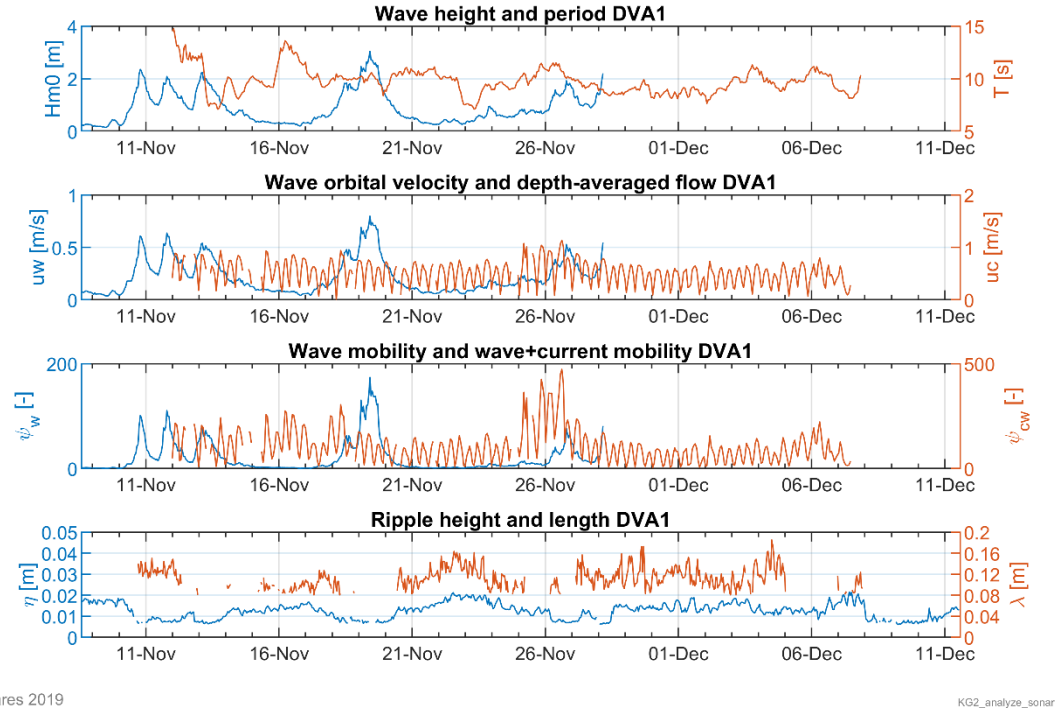

Figure B.5 Timeseries of surface wave characteristics, (wave orbital) velocity, wave and current mobility parameters, and the accompanying bedform dimensions, for DVA-F1.

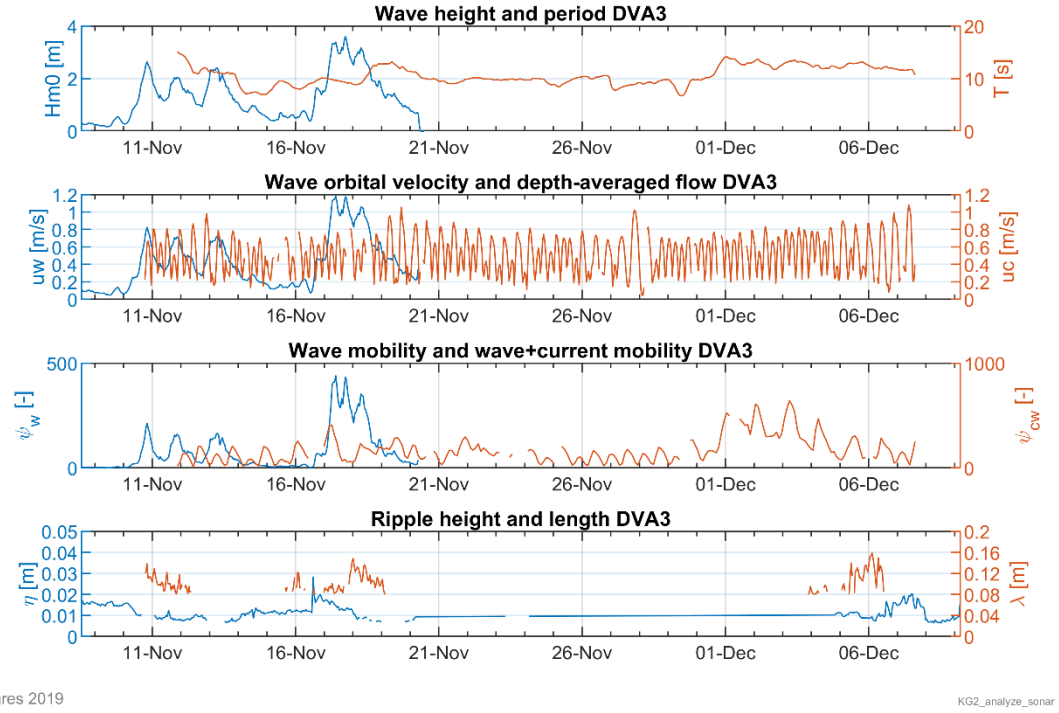

Figure B.6 Timeseries of surface wave characteristics, (wave orbital) velocity, wave and current mobility parameters, and the accompanying bedform dimensions, for AZG-F3.

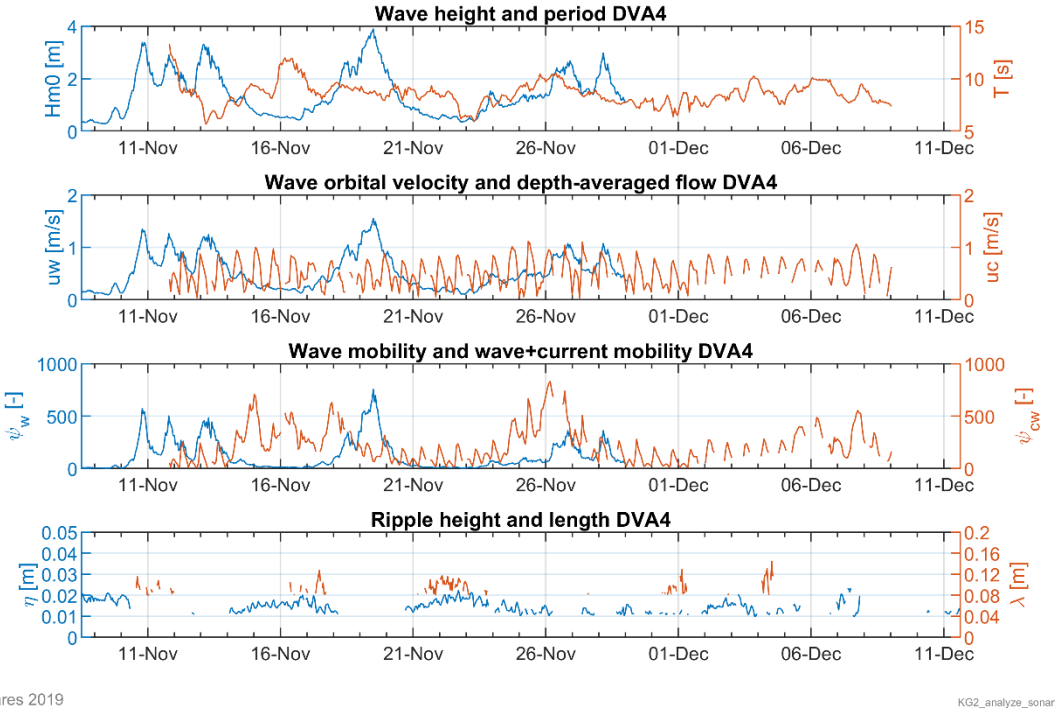

Figure B.7 Timeseries of surface wave characteristics, (wave orbital) velocity, wave and current mobility parameters, and the accompanying bedform dimensions, for DVA-F4.

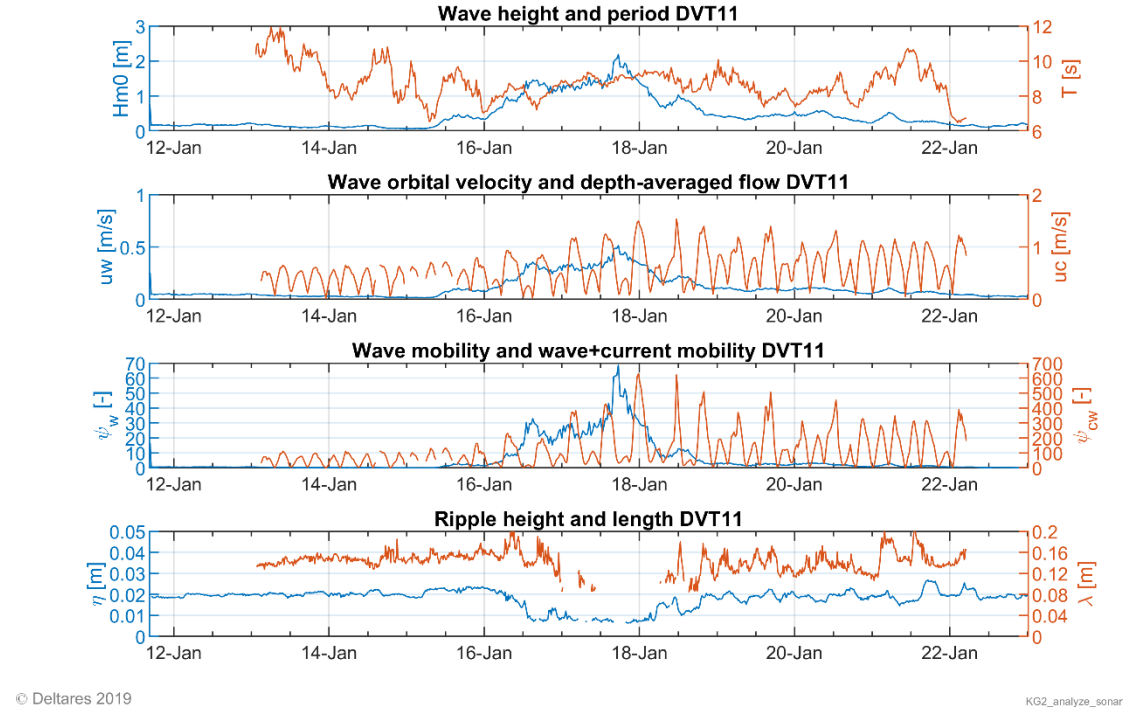

Figure B.8 Timeseries of surface wave characteristics, (wave orbital) velocity, wave and current mobility parameters, and the accompanying bedform dimensions, for DVT1-F1.

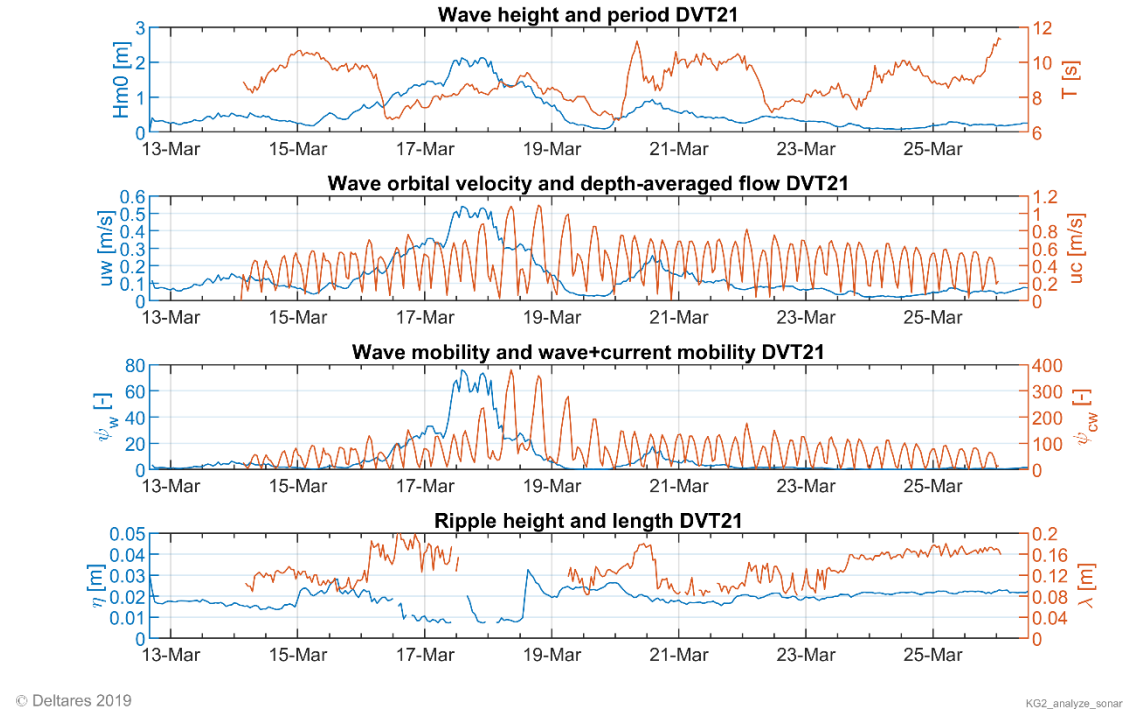

Figure B.9 Timeseries of surface wave characteristics, (wave orbital) velocity, wave and current mobility parameters, and the accompanying bedform dimensions, for DVT2-F1.

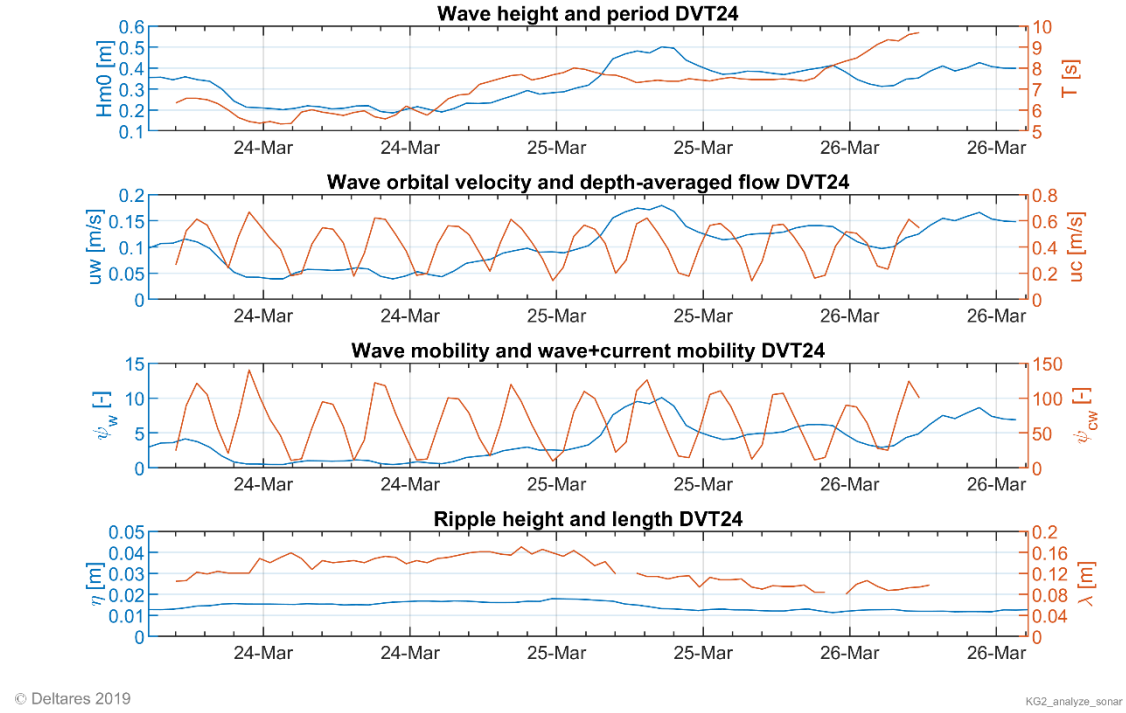

Figure B.10 Timeseries of surface wave characteristics, (wave orbital) velocity, wave and current mobility parameters, and the accompanying bedform dimensions, for DVT2-F1.

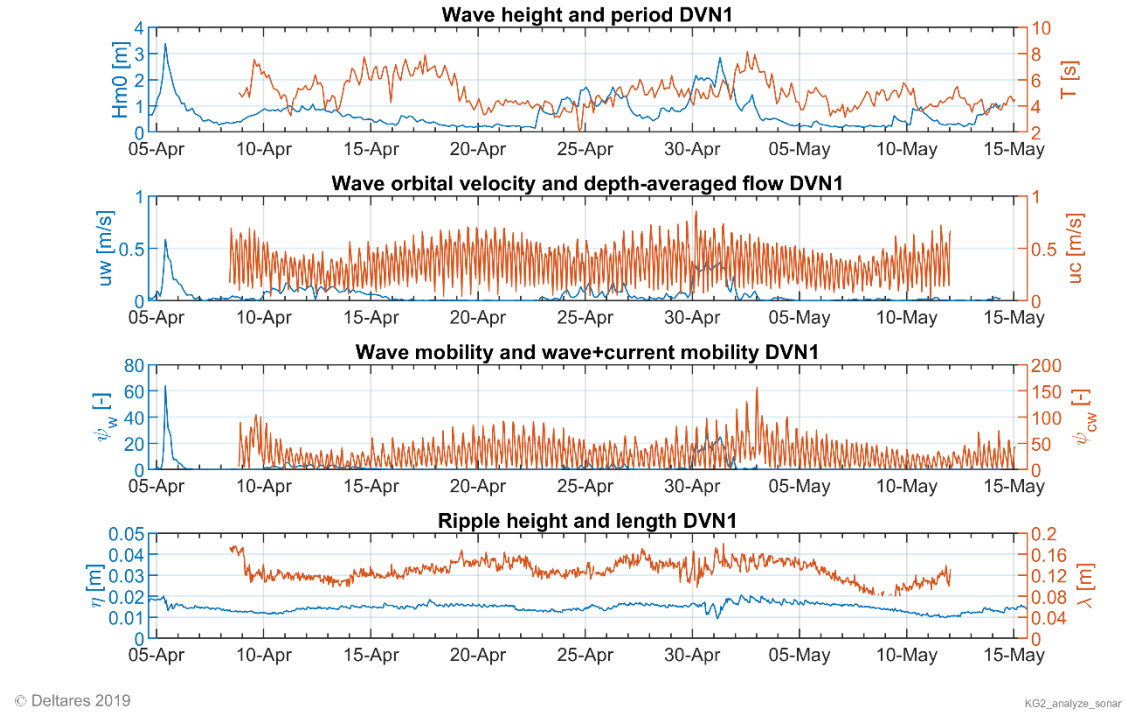

Figure B.11 Timeseries of surface wave characteristics, (wave orbital) velocity, wave and current mobility parameters, and the accompanying bedform dimensions, for DVN-F1.